Molecular Basis for Age-Dependent Microtubule Acetylation by Tubulin Acetyltransferase

Agnieszka Szyk,[1,4] Alexandra M. Deaconescu,[2,4,5] Jeffrey Spector,[1,4] Benjamin Goodman,[1] Max L. Valenstein,[1] Natasza E. Ziolkowska,[1] Vasilisa Kormendi,[1] Nikolaus Grigorieff,[2] and Antonina Roll-Mecak[1,3,*]

[1]Cell Biology and Biophysics Unit, Porter Neuroscience Research Center, National Institute of Neurological Disorders and Stroke, Bethesda, MD 20892, USA
[2]Janelia Farm Research Campus, Howard Hughes Medical Institute, Ashburn, VA 20147, USA
[3]National Heart, Lung and Blood Institute, Bethesda, MD 20892, USA
[4]Co-first author
[5]Present address: Department of Molecular Biology, Cell Biology and Biochemistry, Brown University, Providence, RI 02903, USA
*Correspondence: antonina@mail.nih.gov
http://dx.doi.org/10.1016/j.cell.2014.03.061

SUMMARY

Acetylation of α-tubulin Lys40 by tubulin acetyltransferase (TAT) is the only known posttranslational modification in the microtubule lumen. It marks stable microtubules and is required for polarity establishment and directional migration. Here, we elucidate the mechanistic underpinnings for TAT activity and its preference for microtubules with slow turnover. 1.35 Å TAT cocrystal structures with bisubstrate analogs constrain TAT action to the microtubule lumen and reveal Lys40 engaged in a suboptimal active site. Assays with diverse tubulin polymers show that TAT is stimulated by microtubule interprotofilament contacts. Unexpectedly, despite the confined intraluminal location of Lys40, TAT efficiently scans the microtubule bidirectionally and acetylates stochastically without preference for ends. First-principles modeling and single-molecule measurements demonstrate that TAT catalytic activity, not constrained luminal diffusion, is rate limiting for acetylation. Thus, because of its preference for microtubules over free tubulin and its modest catalytic rate, TAT can function as a slow clock for microtubule lifetimes.

INTRODUCTION

Microtubules are biopolymers constructed by the dynamic association of αβ-tubulin heterodimers and are essential for fundamental cellular processes ranging from intracellular transport to cell division and cellular morphogenesis. Cells constantly adapt their microtubule arrays to physiological needs by modulating the balance between dynamic short-lived, and stable long-lived microtubule subpopulations. For example, during neurite extension, dynamic microtubules drive the growth of a new neurite, while stable microtubules provide the infrastructure to support this cell elongation (Tahirovic and Bradke, 2009). Microtubules are subject to diverse and evolutionarily conserved posttranslational modifications (Garnham and Roll-Mecak, 2012; Wloga and Gaertig, 2010). While the majority of these modifications are on the exterior of the microtubule, acetylation on α-tubulin Lys40 stands out as the only modification in the microtubule lumen and characterizes old, stable microtubules (Greer et al., 1985; L'Hernault and Rosenbaum, 1985; LeDizet and Piperno, 1987; Piperno and Fuller, 1985; Piperno et al., 1987; Schulze et al., 1987). Studies using antibodies specific for acetylated tubulin revealed that acetylation occurs primarily on microtubules and not tubulin and that it is especially abundant on stable microtubules found in cilia, flagella, and centrioles, as well as on subsets of microtubules in the mitotic spindle and long-lived cytoplasmic microtubules with slow dynamics ($t_{1/2} > 2$ hr) that are resistant to depolymerization (Black et al., 1989; Piperno and Fuller, 1985; Piperno et al., 1987; Schulze et al., 1987; Webster and Borisy, 1989). Moreover, stabilization of cellular microtubules using Taxol or microtubule-associated proteins (MAPs) increases acetylation levels (Piperno et al., 1987; Takemura et al., 1992).

Tubulin posttranslational marks, including acetylation, are read by molecular motors and can be used to target them and their cargo to subpopulations of microtubules that have been selectively stabilized (Cai et al., 2009; Hammond et al., 2010). Consequently, tubulin acetylation is important for early polarization events in neurons (Hammond et al., 2010; Reed et al., 2006), and decreased tubulin acetylation is linked to defective axonal transport and neuronal migration as well as neurodegenerative disorders such as Alzheimer's, Huntington's and Charcot-Marie-Tooth diseases (Dompierre et al., 2007; Li et al., 2012; reviewed in Garnham and Roll-Mecak, 2012). Moreover, deficits in axonal transport can be rescued by tubulin hyperacetylation (Dompierre et al., 2007).

Tubulin acetyltransferase (TAT) is required for mechanosensation in Caenorhabditis elegans (Akella et al., 2010; Shida et al., 2010). Acetylation does not seem to be only a passive mark on
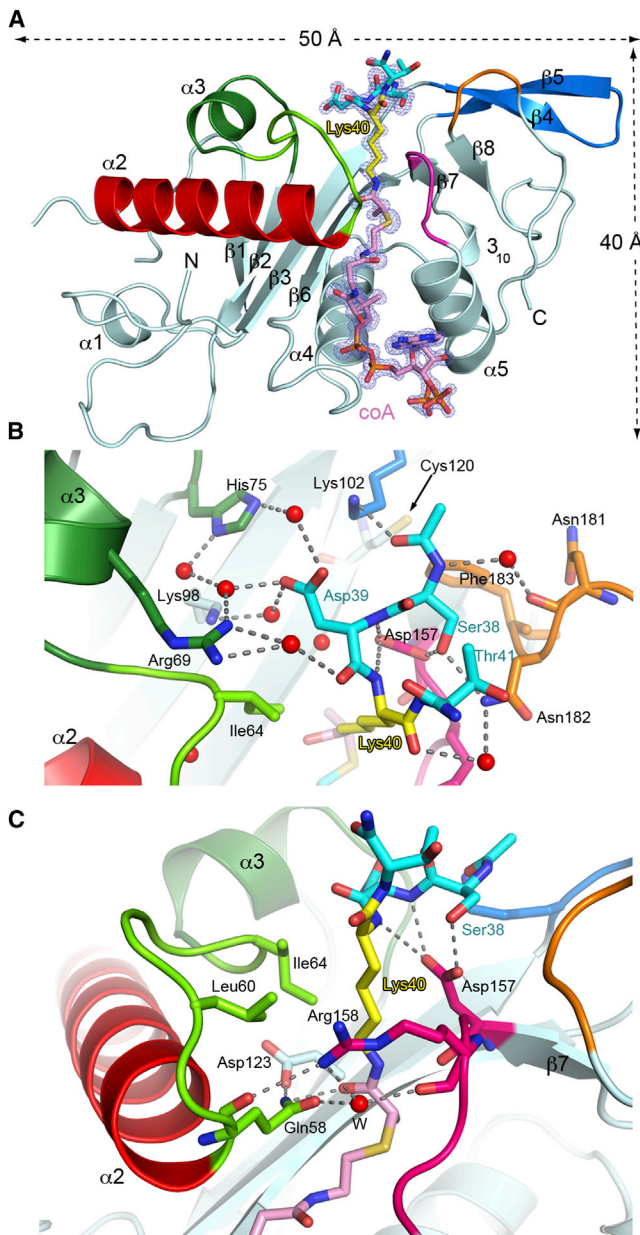
Figure 1. Active Site Architecture and α-Tubulin Lys40 Loop Recognition

(A) Ribbon representation of TAT bound to peptide-coA bisubstrate analog 1 (IC$_{50}$ ~100 μM; Figures S1C and S1D). Analog shown as a stick model with Lys40 yellow, the rest of the peptide moiety, cyan, coA, and linker, pink in the same scheme as Figure S1C. The |F_o|-|F_c| density (prior to modeling the ligand) is contoured at 3.5 σ (blue). Regions engaged in substrate binding and catalysis are colored green, red, magenta, orange, and blue.

(B) Close-up of the active site showing residues engaged in tubulin peptide recognition; red spheres and dashed lines denote water molecules and hydrogen bonds, respectively. Color scheme as in (A). TAT residues labeled in black, peptide residues in color.

(C) Close-up of the active site showing residues important for Lys40 recognition and catalysis. Colored as in (A). Water molecule depicted as a red sphere labeled W.

See also Figure S1 and Table S1.

the microtubule, as its loss disrupts microtubule structural integrity in touch receptor neurons, leading to axonal morphology defects (Cueva et al., 2012; Topalidou et al., 2012). TAT loss also causes brain abnormalities in mice (Kim et al., 2013). Studies in *C. elegans* show that TAT loss disrupts microtubule-based motor transport in axons, leading to spontaneous adult-onset axonal degeneration that worsens with age and axon length (Neumann and Hilliard, 2014).

Other than viruses and clathrin cages, microtubules are the only known hollow polymers in eukaryotic cells. Acetylation on Lys40 stands out as the only known tubulin posttranslational modification located in the microtubule lumen (Nogales et al., 1999; Soppina et al., 2012). To understand the mechanism of any enzyme, it is critical to know how it accesses its substrate. TAT presents a puzzle: its activity is stimulated by microtubules, yet the luminal presentation of Lys40 within microtubules hinders access by the enzyme. How TAT accesses Lys40 in the microtubule lumen is still not understood. It has been proposed that TAT accesses the lumen either by diffusing from ends (Akella et al., 2010) or taking advantage of defects or breathing of the microtubule lattice. The latter would either allow transient access of the enzyme to the lumen or enable excursion of the Lys40 loop to the exterior of the microtubule shaft (Howes et al., 2014; Shida et al., 2010; Yajima et al., 2012). To elucidate substrate access by TAT and to uncover the molecular basis for the in vivo correlation between acetylation and microtubule age, we combined X-ray crystallography, electron microscopy, biochemical and single-molecule fluorescence analyses, and modeling. We report the first crystal structure of TAT in complex with a tubulin peptide-ac-CoA bisubstrate analog that together with structure-based functional analyses constrains the active enzyme to the microtubule lumen. Unexpectedly, we find that acetylation by TAT proceeds stochastically along the microtubule without a preference for ends despite the luminal location of the acetylation site. Consistent with this, single-molecule fluorescence imaging reveals that TAT efficiently and stochastically scans the microtubule, while modeling and kinetic analyses demonstrate that TAT catalytic activity, rather than access to the luminal acetylation site, is rate limiting. Thus, by virtue of its preference for the microtubule geometry and its low catalytic rate, TAT alone can function as an enzymatic timer for microtubule lifetimes.

RESULTS

Tubulin Lys40 Loop Recognition by TAT

Lys40 lies in a 20 amino acid loop (Gigant et al., 2005; Nogales et al., 1998, 1999). Although α-tubulin residues 37–42 are stringently conserved in α-tubulin isoforms with an acetylatable lysine, the ten-residue segment encompassing Lys40 is disordered in cryoelectron microscopy (cryo-EM) reconstructions of microtubules, indicating high flexibility. To visualize at atomic resolution the conformation of the Lys40 loop when engaged by TAT, and to characterize the Lys40 loop-binding surface of the enzyme, we determined the first structures of human TAT (1–196) bound to its substrate lysine, by cocrystallizing it with two distinct bisubstrate analogs consisting of a substrate peptide covalently linked to CoA through Lys40 (Figure 1, Figure S1
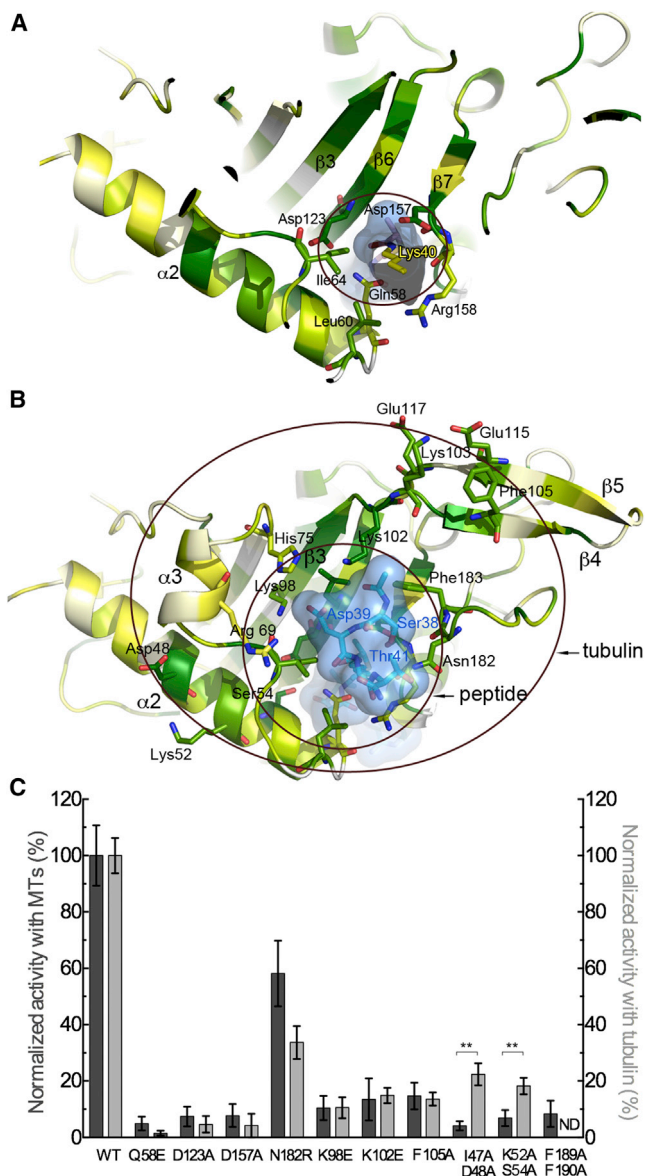
A

B

C

Figure 2. Molecular Determinants for Lys40 Loop and Tubulin Recognition

(A) A slice through TAT shown in ribbon representation color-coded for conservation on a gradient from white (40% identity) to green (100% identity). The tubulin peptide bisubstrate analog is shown as a stick model encased in a transparent molecular surface with α-tubulin Lys40 yellow.

(B) Peptide and tubulin binding interface. Inner and outer circles denote interaction surfaces with the Lys40 loop and tubulin, respectively. TAT represented as in (A), TAT residues labeled in black, peptide residues in blue. The Lys40 side chain projects into the plane of the figure and is not visible in this view.

(C) Normalized acetylation activity of structure-guided TAT mutants with microtubules (dark gray) and tubulin (light gray). Error bars indicate SEM (n ≥ 3). **p < 0.01, t test.

See also Figure S2.

available online, and Experimental Procedures). Such analogs have been extensively employed to analyze the catalytic mechanism of other lysine acetyltransferases (e.g., p300/CBP [Liu et al., 2008] and GCN5 [Poux et al., 2002]). In general, bisubstrate analogs have been important tools for understanding the mechanism of enzymes that link two substrates. Our two 1.35 Å resolution complex structures (Table S1) exhibit no significant differences between them (root mean-square deviation [rmsd] = 0.1 Å over all atoms). The high resolution of our structures (coordinate precision ∼0.1 Å) provides detailed insights into TAT recognition of the Lys40 loop.

The TAT core consists of a six-stranded β sheet surrounded by five α helices (Figure 1). The CoA is cradled between strand β6 and helix α5 (Friedmann et al., 2012; Kormendi et al., 2012; Taschner et al., 2012). Our structures now show residues 38–41 of the α-tubulin acetylation loop folding as an irregular turn (Figure 1B), packing against a funnel-shaped depression in the TAT surface (Figures 2A and 2B), and presenting a fully extended Lys40 into the active site (Figure 1C). The external margin of the TAT funnel is formed by residues from the α2-α3 loop, α3, the loop preceding β8, and the β7-α5 loop (Figure 1A) that make direct and water-mediated hydrogen bonds with the substrate peptide (Figure 1B).

Asp157 of TAT plays a key role at the enzyme-tubulin interface, coordinating the tubulin peptide backbone via a bidentate hydrogen bond to the backbone amides of α-tubulin Asp39 and Lys40 (Figure 1B). Consistent with this, mutation of TAT Asp157 reduces acetylation by ∼96% and ∼92% with tubulin and microtubules, respectively (Figure 2C). The Lys40 backbone is further stabilized by a water-mediated hydrogen bond between its main-chain carbonyl and the side chain of conserved Asn182 of TAT (Figure 1B). Mutation of TAT residues Arg69, His75, and Lys98, which stabilize α-tubulin Asp39, significantly impairs activity (Taschner et al., 2012) (Figure 2C). Likewise, mutation of invariant Asn182 of TAT, which hydrogen-bonds with α-tubulin Ser38, is detrimental (Figures 1B and 2C). The many water-mediated interactions between the α-tubulin peptide and TAT suggest a labile interface, consistent with TAT's modest affinity for and activity with the tubulin peptide (Figure S1B). The peptide N terminus is cradled by invariant Phe183 and Leu104 of TAT, while the carbonyl oxygen preceding α-tubulin Ser38 hydrogen bonds with invariant Lys102. Mutation of Lys102 renders TAT inactive with α-tubulin peptide (data not shown) and reduces its activity ∼87% with tubulin and microtubules (Figure 2C). The extended Lys40 projects into the funnel neck lined by conserved TAT residues (Figures 1C and 2A). Direct and water-mediated hydrogen bonds between invariant Gln58 and Arg158 of TAT close the front of the funnel. The Lys40 side chain is stabilized by van der Waals contacts with conserved Ile64 and the aliphatic moieties of invariant Arg158 and Asp157. Consistent with their role in Lys40 coordination, mutation of Arg158 and Ile64 reduce TAT activity by ∼70% and >90%, respectively (Taschner et al., 2012).

Active Site Architecture

To be acetylated, the ε-ammonium group of Lys40 needs to be deprotonated. This is followed by nucleophilic attack by the amine on the carbonyl carbon of ac-CoA. The invariant Asp157
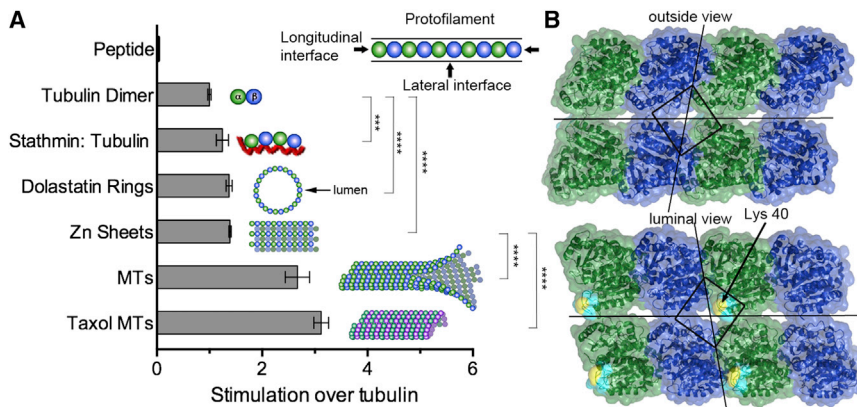
Figure 3. TAT Activity Is Enhanced Predominantly by Lateral Lattice Interactions

(A) TAT activity with tubulin substrates of diverse geometries schematically represented with α- and β-tubulin as green and blue spheres, respectively. Stathmin, shown as red line. MTs, non-Taxol stabilized glycerol microtubules; Taxol MTs, microtubules stabilized with 20 μM Taxol. The presence of dolastatin-10 rings, Zn sheets, and microtubules under the reaction conditions was confirmed by negative stain EM (Figure S3A). Error bars indicate SEM (n ≥ 3). ***p < 0.001, ****p < 0.0001, t test.

(B) Outer and luminal surface of two microtubule protofilaments; α- and β-tubulin, colored green and blue, respectively; the modeled Lys40 loop (visible only in the luminal view) is shown in cyan with Lys40 in yellow. Lines bisecting the surface indicate longitudinal and lateral microtubule lattice interfaces. The square surrounds the vertex of four tubulin subunits that overlies the Lys40 loop.

of TAT is well positioned to deprotonate the Lys40 ε-ammonium as it enters the hydrophobic substrate tunnel. Thus, Asp157 may play a role not only in substrate binding, but also catalysis, consistent with the severely deleterious effects of its mutation (Figure 2C). Further catalysis could be achieved by enhancing nucleophilicity of the amine by a general base. Cys120 was proposed to act as a catalytic residue (Friedmann et al., 2012). Our structure shows that Cys120 approaches no closer than 10.6 Å the amide of the bisubstrate analog (Figure 1B), making it an unlikely catalytic residue. Gln58, also proposed to be a catalytic residue (Taschner et al., 2012) is well positioned to hydrogen bond to the transition state (its side chain amide oxygen lies 2.9 Å from the carbonyl oxygen of the bisubstrate analog linker). It is, however, unlikely to function in deprotonating the incoming α-tubulin Lys40, because its mutation to glutamate, a better base, abolishes TAT activity (Figure 2C). Moreover, while conserved across vertebrate TATs, Gln58 is replaced by Leu in nematode TAT. Gln58 is stabilized by Asp123 whose mutation also decreases TAT activity to background levels (Figure 2C). Asp123 is unlikely to deprotonate Lys40, because it approaches no closer than 5.5 Å from the Lys40 nitrogen atom and is more likely important in orienting the Gln58 side chain. Overall, consistent with the low catalytic rate exhibited with tubulin (0.4 hr^{-1}), our structure shows that the active site of TAT is not optimized for efficient proton transfer.

The TAT-Tubulin Intermolecular Interface

The Lys40 portal bisects a belt of conserved residues on the TAT surface (Figures 2B and S2) that extends beyond the Lys40 loop recognition funnel and likely constitutes an interaction surface with the rest of tubulin and the microtubule. This surface is flanked by helix α2 and the β4-β5 hairpin, a structural element unique to the TAT family and not found in the related GCN5 family acetyltransferases (Friedmann et al., 2012; Kormendi et al., 2012; Taschner et al., 2012). Mutation of conserved Phe189 and Phe190 that support the β4-β5 hairpin reduces TAT activity to background (Figure 2C). Mutation of invariant Phe105 protruding from the β4-β5 hairpin (Figure 2B) severely impairs enzyme

activity with both tubulin and microtubules while still preserving 89% activity with a 15-residue tubulin peptide (data not shown), implicating this residue in tubulin recognition beyond the Lys40 loop. Interestingly, mutation of conserved residues in helix α2 (I47A, D48A and K52A, S54A) impairs acetylation disproportionately with microtubules over tubulin, indicating that this structural element is important for sensing the microtubule. α2 contains one of the most conserved TAT sequence segments, underscoring its functional importance.

Lateral Lattice Interactions Dominate Microtubule Enhancement of TAT Activity

TAT activity is enhanced with microtubules over tubulin (Akella et al., 2010; Kormendi et al., 2012; Maruta et al., 1986; Shida et al., 2010). Microtubules grow through the longitudinal head-to-tail association of tubulin dimers into protofilaments and through lateral interactions, protofilaments associate side-by-side into the cylindrical microtubule. As a step toward localizing the site of TAT action, we sought to identify the microtubule lattice contacts critical for this enhancement. The Lys40 loop lies at the vertex of four tubulin heterodimers in the microtubule (Nogales et al., 1999). Thus, TAT activity can be impacted by both longitudinal (between tubulin heterodimers in a protofilament) and lateral (between neighboring protofilaments) lattice contacts (Figure 3). To understand the relative contribution of longitudinal versus lateral contacts for TAT function, we compared TAT activity on microtubules and on tubulin polymers with distinctly different geometries generated using either peptides or certain cations. All these polymers involve longitudinal interactions between tubulin dimers and a varying interdimer angle and polymer curvature (Figure 3A). Stathmin/Op18 strings two tubulin dimers head to tail (α1β1-α2β2) in a slightly curved configuration (Gigant et al., 2005). Dolastatin-10, a short peptide, induces tubulin rings by curving individual protofilaments such that their luminal surface becomes exposed on the exterior face of the ring (Mulder et al., 2009). Zn^{2+} induces the formation of tubulin sheets in which protofilaments of alternating polarity are arrayed in parallel (Nogales et al., 1998). Acetylation assays

with these substrates revealed a statistically significant enhancement over unpolymerized tubulin, indicating a minor contribution of longitudinal lattice contacts to TAT stimulation by microtubules, as well as a lack of strong curvature dependence (Figure 3A).

The largest activity enhancement over unpolymerized tubulin is seen with microtubules, which unlike the other polymers tested, display lateral interactions in addition to longitudinal ones. TAT's preference for microtubules manifests itself in both enhanced catalytic rate and higher affinity (Figures 3A and S3). While stable complex formation between unpolymerized tubulin and TAT was undetectable by analytical ultracentrifugation at TAT concentrations as high as 40 μM, binding of TAT to microtubules was evident in sedimentation assays, albeit with a modest affinity (K_d ∼44 μM; Figures S3B and S3C), comparable to the reported K_m for the enzyme (∼32 μM) (Friedmann et al., 2012). Consistent with the importance of lateral interactions for TAT binding, we find that the enzyme promotes stacking of dolastatin-induced tubulin rings in a dose-dependent manner (Figures S3D) as previously found for kinesin-13, which is thought to interact with adjacent protofilaments while promoting microtubule depolymerization (Mulder et al., 2009). The F105A TAT mutant defective in acetylation is also impaired in stack formation (Figure S3E). The relatively high TAT concentration needed for stack formation is consistent with the modest affinity of TAT for the microtubule. Interestingly, in *C. elegans* mechanosensory neurons, TAT is one of the most highly expressed genes, at levels comparable to tubulin (Topalidou et al., 2012; Zhang et al., 2002).

Steric Constraints on Lys40 Recognition

Our structures reveal the conformation of the Lys40 loop when engaged by TAT and thus provide constraints on its presentation to the enzyme in the microtubule context. Residues 38–47 of α-tubulin are invisible in current EM reconstructions of microtubules (Fourniol et al., 2010; Maurer et al., 2012), but reliable density is present for Pro37. Pro37 is more than 25 Å from the outside microtubule surface, and just two residues away from Lys40 (a maximum span of 12 Å were the polypeptide fully stretched), implying that Lys40 cannot reach out of the lumen without significant rearrangements in microtubule structure (Figure 3B). Deuterium exchange experiments revealed no differences in regions flanking the Lys40 loop in tubulin versus microtubules (Xiao et al., 2006), underscoring the stability of these secondary structure elements. The Lys40 loop lies beneath a fenestration at the vertex formed by four tubulin dimers (Figure 3B). It has been proposed that this fenestration could allow access of TAT to Lys40 from the outside of the microtubule (Yajima et al., 2012). However, accessing Lys40 from the outside would still require a long, convex protuberance. Importantly, the TAT microtubule recognition surface, defined by our structures and functional analyses is concave, thus not satisfying shape-complementarity principles. Thus, our structural and functional data suggest that large rearrangements of the microtubule or TAT would be needed in order for TAT to reach Lys40 from the microtubule exterior. We cannot completely rule out transient, large openings in the lattice that could expose enough of the luminal space to allow TAT to bind Lys40 without completely entering the lumen as previously proposed (Shida et al., 2010).

However, our experiments with tubulin polymers of different geometries show that lateral lattice interactions are key to TAT activity. These interactions would not be present at microtubule lattice openings.

TAT Acetylation Is Stochastic along the Microtubule

Based on the luminal location of the acetylation site, it was proposed that TAT activity on microtubules would be impaired due to hindered access to Lys40 (Akella et al., 2010; Odde, 1998; Shida et al., 2010). This model is consistent with studies showing that acetylation of axonemes proceeds as a gradient from microtubule ends (Akella et al., 2010), suggestive of a diffusive mechanism along their axis. Interestingly, acetylation on microtubules in cells does not show a gradient from microtubule ends and appears randomly distributed. To elucidate TAT's direct contribution to these observed acetylation patterns, we visualized the distribution of acetylation marks introduced by recombinant TAT in vitro on microtubules using an antibody specific for acetylated tubulin. We find that TAT acetylates along the entire microtubule without a preference for ends (Figure 4). The slow accumulation of acetylation marks on microtubules (over tens of minutes) is consistent with the low acetylation rate observed in bulk measurements (∼1.6 hr^{-1}) as well as cells (Piperno et al., 1987). The longitudinally unbiased, punctate acetylation pattern is similar to that observed on microtubules in cells (Piperno et al., 1987; Webster and Borisy, 1989). We also observe a stochastic distribution of acetylation on non-Taxol stabilized microtubules indicating that this effect cannot be attributed to Taxol (Figure S4). Furthermore, we examined the acetylation distribution under conditions where TAT is not limiting. Early time points show again that the enzyme accesses different sites along the entire microtubule equally well and without a bias for sites close to the ends or restricted regions that could signal lattice defects (Figure 4C). This is apparent in the line-scan of a microtubule at an early time point and also in average line-scans of multiple microtubules, which demonstrate a uniform acetylation probability along the microtubule (Figure 4D).

TAT Scans the Microtubule Lumen Using Surface Diffusion

To understand the mechanism underlying the unbiased acetylation distribution on microtubules and to understand how TAT is able to access the luminal acetylation site, we examined the dynamics of TAT on microtubules. We employed single-molecule total internal reflection fluorescence (TIRF) microscopy to visualize purified TAT-GFP on microtubules immobilized on coverslips (TAT-GFP activity is comparable to that of the untagged protein; Figure S5). We observe that single TAT-GFP molecules scan microtubules bidirectionally with a mean 1D diffusion coefficient of 0.27 μm^2/s (Figures 5A and 5B; Movies S1 and S2). The average interaction time (τ) of TAT-GFP on microtubules is 1.5 s (Figure 5C) and the average microtubule length scanned by a TAT molecule is 2.9 μm, with excursions up to 10.4 μm (Figure S5B). The positions where TAT-GFP molecules start their scans are randomly distributed on the microtubule, showing no bias for ends (Figures 5D and S5C). Two possible explanations for this observation are (1) TAT scans the outside of the microtubule in order to more efficiently find ends or lattice defects that
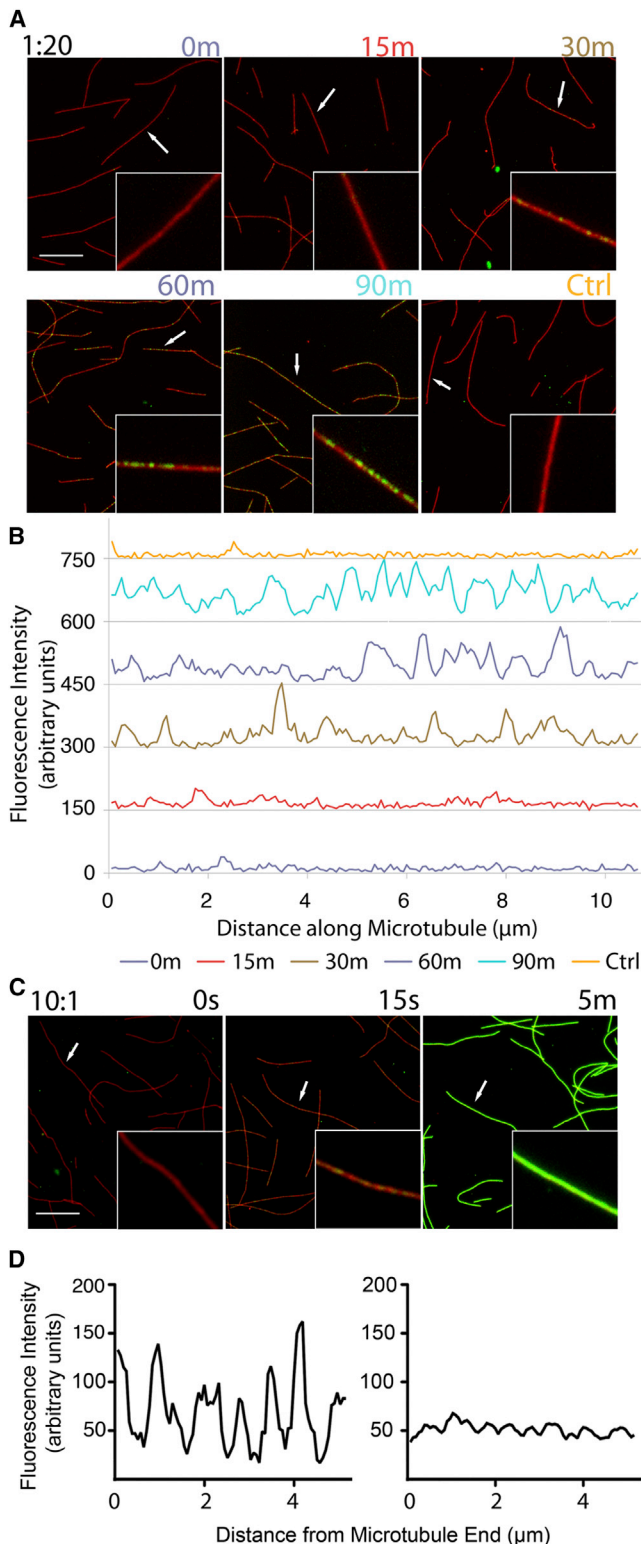
Figure 4. Acetylation Occurs Stochastically along the Microtubule and Is Not Biased for Microtubule Ends

(A) Time course of Taxol stabilized microtubules stained for tubulin (red) and acetylated tubulin (green) after exposure to TAT at 1:20 TAT: tubulin

molar ratio. Insets: close-ups of selected microtubules (arrows). Scale bar represents 5 μm.

(B) Line-scans of selected microtubules (arrows) from (A) in the acetylated tubulin channel. Line-scans from successive time points are staggered vertically by 150 units for clarity.

(C) Time course of Taxol microtubules exposed to excess TAT at 10:1 TAT:tubulin molar ratio. Insets: close-ups of selected microtubules (arrows). Scale bar represents 5 μm.

(D) Analysis of acetylation near microtubule ends with excess TAT 15 s into the reaction. Left: representative scan of the terminal 5 μm of a microtubule. Right: average of 25 line-scans of microtubule ends from the tip to 5 μm into the microtubule. Scanned microtubules had 10 μm minimum length.
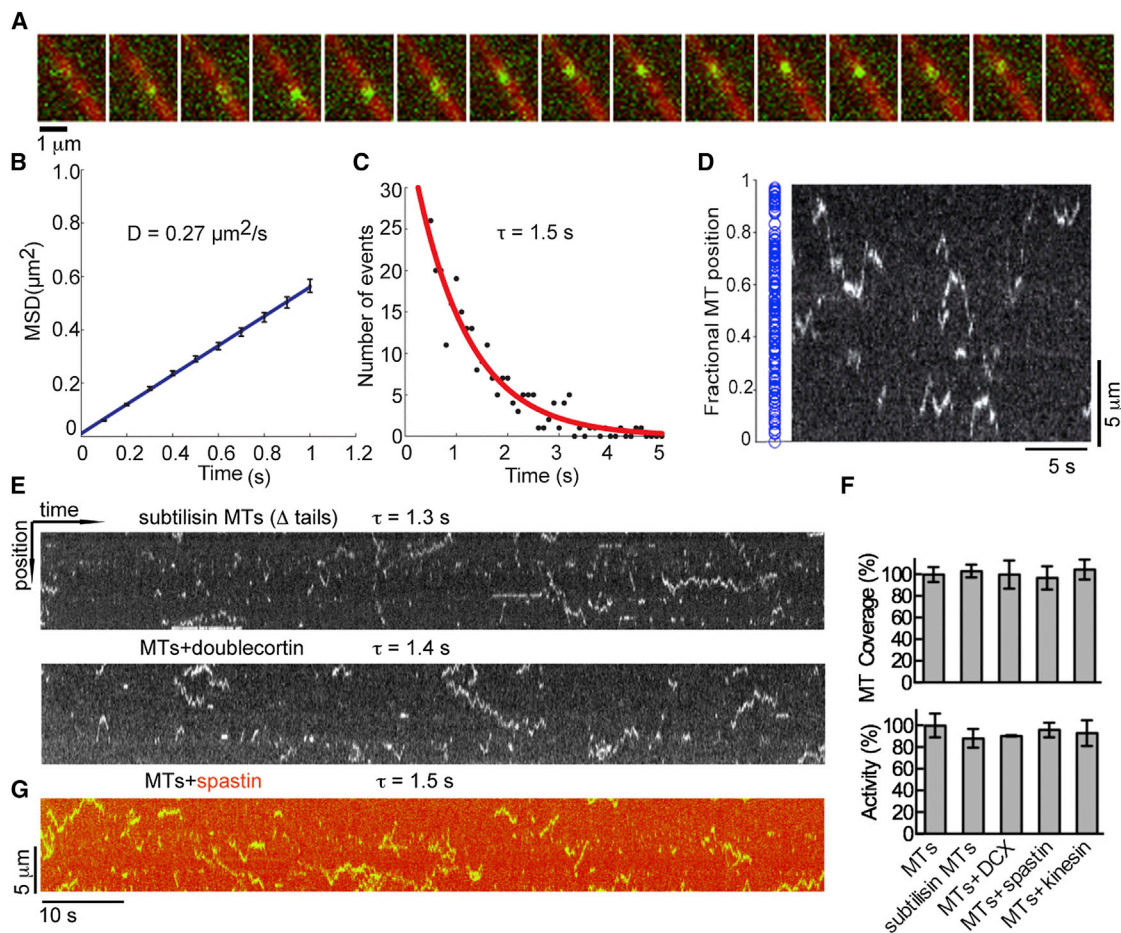
See also Figure S4.

allow it access to the Lys40 loop; TAT access through transient lattice openings has been previously proposed (Howes et al., 2014; Shida et al., 2010), and (2) TAT enters the microtubule lumen through the ends and diffuses through the lumen where it is randomly retarded by its affinity for the microtubule wall. TAT diffusion is too fast to observe when not retarded by the interaction with the microtubule (see below and Experimental Procedures); therefore, the random distribution of scanning start sites would reflect the stochastic distribution of binding events.

Scanning on the microtubule exterior has been observed, among others, for the depolymerizing kinesin MCAK (Helenius et al., 2006) and tau (Hinrichs et al., 2012). MCAK uses this mechanism to find microtubule ends more efficiently (Helenius et al., 2006). One-dimensional diffusion is also used by DNA binding proteins to scan long DNAs for specific sequences (von Hippel and Berg, 1989). TAT robustly scans subtilisin-treated microtubules lacking the tubulin C-terminal tails (Figure 5E), unlike MCAK and tau that use these negatively charged tails for this process (Helenius et al., 2006; Hinrichs et al., 2012). Analysis of 50 microtubules shows that TAT scanning covers the same total microtubule length, regardless of whether microtubules are subtilisin-treated or untreated (Figure 5F, upper panel). A recent study reported a weak effect of the C-terminal tails on TAT microtubule binding (Howes et al., 2014). Here, we find that microtubule acetylation is unaffected by removal of the C-terminal tails (Figure 5F, lower panel). Tubulin C-terminal tails are subject to abundant posttranslational modifications and acetylated microtubules in the cell are often also polyglutamylated, leading to the hypothesis that acetylation can be affected by these other modifications (Howes et al., 2014). However, we find that TAT scans unmodified microtubules and acetylates them as effectively as brain microtubules that are heavily polyglutamylated on C-terminal tails (Figures S5G and S5H). *Saccharomyces cerevisiae* α-tubulin does not have a conserved acetylation loop and TAT is absent in this organism. We do not observe TAT-GFP scanning on purified *S. cerevisiae* microtubules nor on engineered *S. cerevisiae* microtubules in which the divergent endogenous C-terminal tails were replaced with human C-terminal tails (Extended Experimental Procedures).

To establish whether scanning occurs on the outer surface of the microtubule or intraluminally, we decorated the external microtubule surface with three microtubule binding proteins with distinct binding modes (doublecortin, spastin, and the motor domain of kinesin-5) and measured both TAT scanning and acetylation activity (Figures 5 and S5). Doublecortin covers

Figure 5. TAT-GFP Scans the Microtubule

(A) Sequential frames of a TAT-GFP (green) movie. Fifteen frames of a continuous TIRF recording (100 ms frames) were overlaid on one microtubule image (red).

(B) Mean-squared displacement (MSD) of TAT-GFP plotted against time. A linear curve fitted to the shown time interval yields a diffusion coefficient of 0.27 ± 0.01 μm^2/s. Error bars represent SEM.

(C) Distribution of durations of TAT-GFP interactions with the microtubule. An exponential curve fitted to the histogram and corrected for photobleaching (Figure S5A) yields a mean lifetime of interaction (τ) of 1.5 ± 0.3 s (R^2 = 0.91; N = 251).

(D) Initial positions (blue dots) of scanning TAT-GFP along microtubules, N = 163 (left) (Figure S5C); kymograph depicting TAT-GFP motion on a microtubule showing random initial positions along the microtubule (right).

(E) Kymographs depicting the motion of TAT-GFP on a subtilisin-treated microtubule missing C-terminal tails (top) and microtubule in the presence of saturating amounts of doublecortin (bottom) (see also Figure S5K).

(F) Normalized total microtubule length scanned by TAT-GFP molecules (top) and acetylation activity (bottom) with subtilisin microtubules and microtubules coated with doublecortin, spastin, and kinesin-5 motor domain (see also Figure S5J). Error bars indicate SEM.

(G) Kymograph depicting the motion of TAT-GFP on microtubules decorated with DyLight 550-labeled spastin in the presence of ATPγS, which inhibits severing, but not microtubule binding (Roll-Mecak and Vale, 2008). τ, defined as in (C).

the fenestration at the vertices between four tubulin dimers that overlie the Lys40 loop (Fourniol et al., 2010) and that was proposed to allow access of TAT to the microtubule lumen from the outside. Addition of saturating concentrations of doublecortin had no effect on TAT-GFP microtubule scanning (τ = 1.4 s compared to 1.5 s for undecorated microtubules) or acetylation rates (Figures 5E, 5F, and S5K). Interestingly, TAT localizes to doublecortin decorated microtubules in vivo (Kim et al., 2013). Saturating concentrations of spastin or kinesin likewise had no effect (Figures 5F and S5I). Under our experimental conditions, the microtubules were saturated with these MAPs (Figure S5J). We also used Dylight 550-labeled spastin to visualize

microtubule decoration (Figure 5G; Movie S3). Microtubules coated with labeled spastin were also scanned efficiently by TAT (τ = 1.5 s, statistically indistinguishable from that on undecorated microtubules). Maximum intensity projections demonstrate that total microtubule coverage by TAT-GFP was unchanged in the presence of doublecortin, kinesin, or spastin (Figure 5F, upper panel). Together, the results of our experiments with microtubules missing the C-terminal tails as well as decorated with various MAPs argue that TAT-GFP scans the microtubule lumen.

Recent cryoelectron reconstructions revealed Fab fragments (MW ~50 kDa) of IgG 6-11B-1 antibodies against acetylated
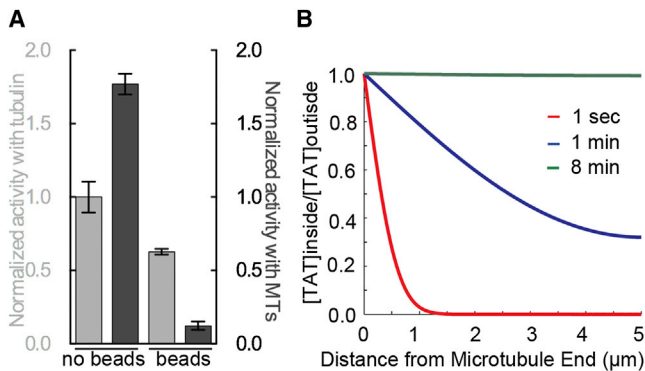
Figure 6. Substrate Access by TAT Is Spatially Constrained, but Not Rate Limiting, for Microtubule Acetylation

(A) Normalized activity of biotinylated TAT, free in solution or immobilized to 1 μm diameter streptavidin beads, with tubulin (light gray) and microtubules (dark gray).

(B) Calculated profiles of TAT diffusion into a microtubule (or probability of residence) at positions along the microtubule at indicated time points (see Extended Experimental Procedures). At 8 min, TAT is completely equilibrated between the lumen of a 10 μm long microtubule and the outside volume. See also Figure S6.

Lys40 arranged in regular arrays inside the microtubule lumen (Soppina et al., 2012). Surprisingly, we find that even larger, full-length IgG 6-11B-1 antibodies can gain access to the lumen of Taxol-stabilized acetylated microtubules. Negative-stain EM of microtubules incubated with these antibodies revealed two distinct populations (Figures S6A–S6E): one had an evident protofilament structure and displayed a 4 nm layerline, reflecting the spacing underlying the helical structure of the microtubule because of the α/β tubulin equivalency at low resolution; the second showed a hardly discernible protofilament structure in real space and an additional 8 nm layerline in Fourier space (Figure S6E) indicative of the antibody binding to the tubulin heterodimer. Decorated microtubules showed no additional density along the edges, indicating that binding occurs on the luminal surface. In contrast, a well-characterized antibody that binds to the outer surface (directed against the α-tubulin C-terminal tail) showed clear density along microtubule edges (Figure S6F). Moreover, 6-11B-1 IgG also clustered at sites of microtubule mechanical damage where the lumen is exposed (Figure S6G). Taken together, these data indicate that an intact IgG antibody with affinity for the Lys40 loop can enter the microtubule.

Because our EM studies show that a particle as large as an antibody (relative dimensions of IgG and our TAT construct shown in Figure S6H) can gain access to the microtubule lumen (inner diameter 15 nm) on a timescale of tens of minutes (comparable to acetylation rates), we coupled a C-terminally biotinylated TAT construct to streptavidin beads 1 μm in diameter (experiments using 200 nm beads yielded the same results; data not shown). We then compared the activity of the bead-coupled TAT with tubulin and microtubules. While the bead-coupled enzyme retained activity with tubulin, activity with microtubules was reduced ~89% (Figure 6A). The residual activity is likely due to unpolymerized tubulin (~15%) present in these experiments. Overall, our experiments with engineered and bead-coupled TAT are consistent

with a requirement for the enzyme to enter a confined space during acetylation, and our experiments with MAP-coated microtubules suggest that TAT is able to scan the luminal microtubule wall using surface diffusion.

We cannot completely rule out that there are defects in the lattice that would allow the enzyme to enter at "breathing" points along the microtubule as proposed (Friedmann et al., 2012; Howes et al., 2014; Shida et al., 2010; Soppina et al., 2012). This could account for the random distribution of acetylation marks as well as TAT trajectories that we observe. Defects on the order of 1–2 nm have been documented in microtubules in vitro at points where there are protofilament number changes (Chrétien et al., 1992); however, these defects are sparse, the spacing between them ranging from 2.6 μm to more than 20 μm (Chrétien et al., 1992), not consistent with the nonbiased acetylation patterns that we see on microtubules. The diameter of the TAT globular core is ~5 nm, imposing a lower bound on the size of these possible defects on the order of at least one tubulin dimer. Notably, microtubule acetylation is especially abundant on cilia and neuronal microtubules that are covered with stabilizing MAPs. In our assays, acetylation or TAT scanning are not impaired on microtubules coated with doublecortin that binds at the vertex of four tubulin dimers and stabilizes longitudinal and lateral lattice interactions. Moreover, TAT mobility (Figure 5) and acetylation patterns (Figure 4) on the microtubule do not show a bias toward specific regions that would suggest lattice defects (Figure S5C).

TAT Catalytic Rate, Not Lys40 Accessibility, Is Rate Limiting

The stochastic distribution of acetylation marks and TAT scanning trajectories argues against access to Lys40 being limiting for microtubule acetylation. We applied a previously derived first-principles model to TAT diffusion that accounts for microtubule wall hindrance effects and reversible binding to describe diffusion through the 15 nm wide microtubule lumen of particles with varying size and microtubule affinity (Bungay and Brenner, 1973; Odde, 1998). Our calculations (Experimental Procedures) indicate that the TAT (Stokes radius R_H = 2.7 nm) equilibration time between the microtubule outside and inside would be on the order of minutes for a 10 μm-long microtubule (open on both ends), the mean length of microtubules in our experiment (Figures 6B and S4E). This is consistent with our observation that, when in excess, TAT acetylates unhindered along the entire microtubule on the order of minutes (Figure 4C). The equilibration time depends primarily on TAT dimensions and affinity for the microtubule wall and is very sensitive to the latter parameter (Odde, 1998) (Experimental Procedures; Figure S6I). Our calculations show that TAT diffusion is retarded three orders of magnitude by luminal confinement and microtubule binding. At our current frame acquisition rates, we are unable to detect TAT-GFP diffusion through the microtubule when TAT is not retarded (calculated $D_{hindered}$ = 26.3 μm²/s, Experimental Procedures). Thus, the random distribution of scanning trajectory starting points (Figure 5D and S5C) most likely reflects the stochastic nature of the TAT-microtubule interaction, i.e., TAT can be observed in our assays only when retarded by its interaction with the microtubule.

DISCUSSION

Stable microtubules in cells, but not dynamic microtubules, are marked by acetylation at Lys40. In the absence of acetylation by TAT, microtubule structural integrity is affected and cell polarity is perturbed in cells that are particularly dependent on stable, polarized microtubule arrays, such as neurons (Cueva et al., 2012; Li et al., 2012; Neumann and Hilliard, 2014; Topalidou et al., 2012). But, how are stable microtubules selectively marked for the action of regulators? Our results indicate that microtubule age-dependent acetylation by TAT is achieved not by impaired diffusion because of the luminal location of the acetylation site, but due to the slow enzymatic rate of TAT that is more than an order of magnitude slower than the lifetime of dynamic microtubules ($t_{1/2}$ ~5 min) and more closely matched to the lifetime of stable microtubules ($t_{1/2}$ > 2 hr) in cells (Schulze et al., 1987; Schulze and Kirschner, 1987; Webster and Borisy, 1989). Acetylation is especially enriched on microtubule populations with extremely slow dynamics ($t_{1/2}$ ~16 hr) (Webster and Borisy, 1989) that are a hallmark of postmitotic cells with complex microtubule architectures such as neurons (Black et al., 1989). The cell solves the problem of selective marking a stable microtubule population by having a modification inside the microtubule lumen and then exploiting the kinetic discordance between the rate of one-dimensional diffusion versus the catalytic constant of the tubulin acetylase. Acetylation is reversed in cells by the action of tubulin deacetylases such as HDAC6 and SIRT2 (Hubbert et al., 2002; North et al., 2003). The accumulation of acetylated stable microtubules in cells implies that the reverse deacetylation reaction is even slower than TAT microtubule acetylation. TAT activity defines the population of microtubules that would be available for deacetylases to act on, i.e., stable microtubules because dynamic microtubules would not persist long enough for TAT to acetylate them. However, the density of the acetylation mark on stable microtubules does depend on the activity of deacetylases. In vivo, deacetylation is strongly coupled with microtubule depolymerization (Black et al., 1989), thus resetting the age-dependent acetylation clock. The net acetylation level and the steepness of the acetylation gradient from old to new will be modulated by overall deacetylase activity. Thus, TAT can function as an enzymatic timer for microtubules with slow turnover and mark them selectively for the action of microtubule regulators.

Our kinetic analyses and modeling show that TAT diffusion is markedly faster than its catalytic rate, explaining the lack of an acetylation gradient on microtubules as would be expected for a diffusion-limited reaction. Consistent with access to the luminal modification site not being limiting, acetylation rates are not enhanced when TAT is copolymerized with tubulin (Kalebic et al., 2013) and acetylation in vivo lags tens of minutes behind microtubule polymerization (Black et al., 1989; Piperno et al., 1987). Earlier experiments show that acetylation is not enhanced when microtubules are shortened by shearing (Maruta et al., 1986). In order to produce an observable gradient, microtubules would have to be sufficiently long to match the catalytic rate of TAT. Such an effect would become observable at microtubule lengths exceeding 75 μm (or 150 μm if both ends are open; Figure S6J). Microtubule lengths in vivo range between 1–100 μm (Odde, 1998). In the shearing experiments the mean lengths were reduced from ~3.4 to 0.6 μm, a length regime where no diffusion limiting effects would have been seen 15 min into the reaction when acetylation was measured (Maruta et al., 1986). Thus, our experiments (Figures 4 and 5) as well as kinetic modeling (Figure 6B) indicate that substrate access through microtubule ends would not be rate limiting for acetylation by TAT, but catalytic rate is. While microtubule defects could further facilitate TAT access to the luminal microtubule space in vivo, they are not required for TAT access on timescales of the order of the catalytic rate of the enzyme. Unlike kinesins that have been shown to act as microtubule rulers by selectively tagging and enhancing their activity on longer microtubules (Subramanian et al., 2013; Varga et al., 2009), TAT can act as a timer for microtubule lifetimes and can effectively mark stable microtubules, both long and short.

Consistent with the slow catalytic rate of the enzyme, our crystal structures of TAT with two bisubstrate analogs reveal an active site not optimized for efficient catalysis (Figures 1, 2, and S1E). To accumulate a Michaelis complex and achieve reactivity in this regime of low k_{cat}, the off-rate of the enzyme would have to be slow. However, in such a situation, the enzyme would have limited coverage of the microtubule length in conditions where TAT is limiting because it would be retained close to the microtubule end. We propose that scanning of the microtubule via surface diffusion allows TAT to remain associated with the microtubule in a reactive state for longer periods and yet achieve coverage of long microtubule spans. The high degree of hydration at the TAT-Lys40 loop interface revealed by our cocrystal structures could facilitate the diffusion along the microtubule, akin to the "water lubricated" 1D diffusion proposed to be important for the diffusion of DNA binding proteins along DNA (Cooper and Wordeman, 2009).

Electron cryotomography revealed discrete, closely spaced particles decorating the lumen of flagellar (Nicastro et al., 2006; Sui and Downing, 2006) and neuronal (Garvalov et al., 2006; Topalidou et al., 2012) microtubules. Future experiments will clarify how TAT access is modulated by the presence of luminal particles. Interestingly, these particles disappear from the lumen of neuronal microtubules upon rapid disassembly and reassembly (Burton, 1984), suggesting a microtubule age-dependent accumulation process. In addition to providing a molecular basis for age-dependent microtubule acetylation, our studies are also applicable to the microtubule binding behavior of other proteins with luminal localization found in neuronal microtubules and axonemes. Furthermore, the interplay between TAT acetylation activity in the constrained luminal space and the association of the enzyme with larger complexes in the cell will be an interesting area of future exploration.

EXPERIMENTAL PROCEDURES

Protein Production, Crystallization, and X-Ray Structure Determination

Homo sapiens TAT (1–196) was expressed in *Escherichia coli* as a GST-fusion and purified by standard chromatography techniques. A reversed-phase high-performance liquid chromatography (HPLC) assay shows that TAT acetylates minimal tubulin-derived peptides, albeit at a rate lower than with tubulin (Figures S1A and S1B), demonstrating that the minimal requirements for

catalysis are satisfied by the engagement of TAT with an α-tubulin-derived peptide. The existence of a ternary complex between TAT, ac-CoA, and its tubulin substrate is supported by previous kinetic analyses (Friedmann et al., 2012), justifying the use of bisubstrate analogs as functional mimics of a TAT ternary complex. Two bisubstrate analogs (Figures S1C and S1D) yielded cocrystals that diffracted to better than 1.35 Å resolution. Details for crystallization, structure determination, and purification of TAT constructs can be found in Extended Experimental Procedures.

Acetylation Assays

Tubulin and microtubule acetylation assays with various mutants were performed using ^{3}[H]acetyl-coA as in Kormendi et al. (2012). Acetylation assays with peptides, various tubulin polymers, in the presence of MAPs as well as bead-coupled TAT are described in Extended Experimental Procedures.

Modeling TAT Diffusion

To assess the diffusion rate of TAT inside the microtubule, we used a previously developed mathematical model (Bungay and Brenner, 1973; Odde, 1998) that approximates the diffusing molecule as a sphere in a cylindrical pore and accounts for translational diffusion, hindrance due to the microtubule wall, and the reversible binding of the molecule to the microtubule at dilute concentrations below K_d. Details of the calculations can be found in Extended Experimental Procedures. The free diffusion coefficient of TAT is 79.3 μm^2/s. This indicates that a single TAT molecule travels an root mean-square (rms) distance of 3.9 μm in ~0.1 s. TAT diffusion inside a microtubule is further hindered by the microtubule wall, resulting in a $D_{hindered}$ of 26.3 μm^2/s (2.3 μm traveled in 0.1 s), given by the Bungay-Brenner relationship (Bungay and Brenner, 1973). TAT diffusion is most significantly retarded by its reversible binding to the microtubule wall (Odde, 1998). This results in an effective diffusion constant of TAT $D_{effective}$ ~0.082 μm^2/s.

TIRF Imaging and Analysis

Chambers for single molecule assays were assembled as described in Ziółkowska and Roll-Mecak (2013). GFP-TAT molecules were tracked using MTrackJ (Meijering et al., 2012). A complete description of data collection and analyses can be found in Extended Experimental Procedures.

ACCESSION NUMBERS

The Protein Data Bank accession numbers for the atomic coordinates and structure factor amplitudes reported in this paper are 4PK2 and 4PK3.

SUPPLEMENTAL INFORMATION

Supplemental Information includes Extended Experimental Procedures, six figures, three movies, and one table and can be found with this article online at http://dx.doi.org/10.1016/j.cell.2014.03.061.

AUTHOR CONTRIBUTIONS

A.R.-M. conceived the project and planned experiments together with all authors. A.S. solved structures together with A.R.-M. and performed activity assays. A.M.D. performed EM and interpreted data together with N.G. J.S. performed TIRF assays and diffusion calculations. B.G. performed immunofluorescence. M.L.V. performed TIRF assays with MAPs and yeast microtubules. N.E.Z. performed microtubule binding assays. A.R.-M. wrote the manuscript with help from A.M.D. and J.S. The manuscript was reviewed by all authors.

ACKNOWLEDGMENTS

REFERENCES

Akella, J.S., Wloga, D., Kim, J., Starostina, N.G., Lyons-Abbott, S., Morrissette, N.S., Dougan, S.T., Kipreos, E.T., and Gaertig, J. (2010). MEC-17 is an alpha-tubulin acetyltransferase. Nature 467, 218–222.

Bechstedt, S., and Brouhard, G.J. (2012). Doublecortin recognizes the 13-protofilament microtubule cooperatively and tracks microtubule ends. Dev. Cell 23, 181–192.

Black, M.M., Baas, P.W., and Humphries, S. (1989). Dynamics of alpha-tubulin deacetylation in intact neurons. J. Neurosci. 9, 358–368.

Bungay, P.M., and Brenner, H. (1973). The motion of a closely-fitting sphere in a fluid-filled tube. Int. J. Multiph. Flow 1, 25–56.

Burton, P.R. (1984). Luminal material in microtubules of frog olfactory axons: structure and distribution. J. Cell Biol. 99, 520–528.

Cai, D., McEwen, D.P., Martens, J.R., Meyhofer, E., and Verhey, K.J. (2009). Single molecule imaging reveals differences in microtubule track selection between Kinesin motors. PLoS Biol. 7, e1000216.

Chrétien, D., Metoz, F., Verde, F., Karsenti, E., and Wade, R.H. (1992). Lattice defects in microtubules: protofilament numbers vary within individual microtubules. J. Cell Biol. 117, 1031–1040.

Cooper, J.R., and Wordeman, L. (2009). The diffusive interaction of microtubule binding proteins. Curr. Opin. Cell Biol. 21, 68–73.

Cueva, J.G., Hsin, J., Huang, K.C., and Goodman, M.B. (2012). Posttranslational acetylation of α-tubulin constrains protofilament number in native microtubules. Curr. Biol. 22, 1066–1074.

Dompierre, J.P., Godin, J.D., Charrin, B.C., Cordelières, F.P., King, S.J., Humbert, S., and Saudou, F. (2007). Histone deacetylase 6 inhibition compensates for the transport deficit in Huntington's disease by increasing tubulin acetylation. J. Neurosci. 27, 3571–3583.

Fourniol, F.J., Sindelar, C.V., Amigues, B., Clare, D.K., Thomas, G., Perderiset, M., Francis, F., Houdusse, A., and Moores, C.A. (2010). Template-free 13-protofilament microtubule-MAP assembly visualized at 8 A resolution. J. Cell Biol. 191, 463–470.

Friedmann, D.R., Aguilar, A., Fan, J., Nachury, M.V., and Marmorstein, R. (2012). Structure of the α-tubulin acetyltransferase, αTAT1, and implications for tubulin-specific acetylation. Proc. Natl. Acad. Sci. USA 109, 19655–19660.

Garnham, C.P., and Roll-Mecak, A. (2012). The chemical complexity of cellular microtubules: tubulin post-translational modification enzymes and their roles in tuning microtubule functions. Cytoskeleton (Hoboken) 69, 442–463.

Garvalov, B.K., Zuber, B., Bouchet-Marquis, C., Kudryashev, M., Gruska, M., Beck, M., Leis, A., Frischknecht, F., Bradke, F., Baumeister, W., et al. (2006). Luminal particles within cellular microtubules. J. Cell Biol. 174, 759–765.

Gigant, B., Wang, C., Ravelli, R.B., Roussi, F., Steinmetz, M.O., Curmi, P.A., Sobel, A., and Knossow, M. (2005). Structural basis for the regulation of tubulin by vinblastine. Nature 435, 519–522.

Greer, K., Maruta, H., L'Hernault, S.W., and Rosenbaum, J.L. (1985). Alpha-tubulin acetylase activity in isolated Chlamydomonas flagella. J. Cell Biol. 101, 2081–2084.

Hammond, J.W., Huang, C.F., Kaech, S., Jacobson, C., Banker, G., and Verhey, K.J. (2010). Posttranslational modifications of tubulin and the polarized transport of kinesin-1 in neurons. Mol. Biol. Cell 21, 572–583.

Helenius, J., Brouhard, G., Kalaidzidis, Y., Diez, S., and Howard, J. (2006). The depolymerizing kinesin MCAK uses lattice diffusion to rapidly target microtubule ends. Nature 441, 115–119.

Hinrichs, M.H., Jalal, A., Brenner, B., Mandelkow, E., Kumar, S., and Scholz, T. (2012). Tau protein diffuses along the microtubule lattice. J. Biol. Chem. *287*, 38559–38568.

Howes, S.C., Alushin, G.M., Shida, T., Nachury, M.V., and Nogales, E. (2014). Effects of tubulin acetylation and tubulin acetyltransferase binding on microtubule structure. Mol. Biol. Cell *25*, 257–266.

Hubbert, C., Guardiola, A., Shao, R., Kawaguchi, Y., Ito, A., Nixon, A., Yoshida, M., Wang, X.F., and Yao, T.P. (2002). HDAC6 is a microtubule-associated deacetylase. Nature *417*, 455–458.

Kalebic, N., Martinez, C., Perlas, E., Hublitz, P., Bilbao-Cortes, D., Fiedorczuk, K., Andolfo, A., and Heppenstall, P.A. (2013). Tubulin acetyltransferase αTAT1 destabilizes microtubules independently of its acetylation activity. Mol. Cell. Biol. *33*, 1114–1123.

Kim, G.W., Li, L., Gorbani, M., You, L., and Yang, X.J. (2013). Mice lacking α-tubulin acetyltransferase 1 are viable but display α-tubulin acetylation deficiency and dentate gyrus distortion. J. Biol. Chem. *288*, 20334–20350.

Kormendi, V., Szyk, A., Piszczek, G., and Roll-Mecak, A. (2012). Crystal structures of tubulin acetyltransferase reveal a conserved catalytic core and the plasticity of the essential N terminus. J. Biol. Chem. *287*, 41569–41575.

L'Hernault, S.W., and Rosenbaum, J.L. (1985). Chlamydomonas alpha-tubulin is posttranslationally modified by acetylation on the epsilon-amino group of a lysine. Biochemistry *24*, 473–478.

LeDizet, M., and Piperno, G. (1987). Identification of an acetylation site of Chlamydomonas alpha-tubulin. Proc. Natl. Acad. Sci. USA *84*, 5720–5724.

Li, L., Wei, D., Wang, Q., Pan, J., Liu, R., Zhang, X., and Bao, L. (2012). MEC-17 deficiency leads to reduced α-tubulin acetylation and impaired migration of cortical neurons. J. Neurosci. *32*, 12673–12683.

Liu, X., Wang, L., Zhao, K., Thompson, P.R., Hwang, Y., Marmorstein, R., and Cole, P.A. (2008). The structural basis of protein acetylation by the p300/CBP transcriptional coactivator. Nature *451*, 846–850.

Maruta, H., Greer, K., and Rosenbaum, J.L. (1986). The acetylation of alpha-tubulin and its relationship to the assembly and disassembly of microtubules. J. Cell Biol. *103*, 571–579.

Maurer, S.P., Fourniol, F.J., Bohner, G., Moores, C.A., and Surrey, T. (2012). EBs recognize a nucleotide-dependent structural cap at growing microtubule ends. Cell *149*, 371–382.

Meijering, E., Dzyubachyk, O., and Smal, I. (2012). Methods for cell and particle tracking. Methods Enzymol. *504*, 183–200.

Mulder, A.M., Glavis-Bloom, A., Moores, C.A., Wagenbach, M., Carragher, B., Wordeman, L., and Milligan, R.A. (2009). A new model for binding of kinesin 13 to curved microtubule protofilaments. J. Cell Biol. *185*, 51–57.

Neumann, B., and Hilliard, M.A. (2014). Loss of MEC-17 leads to microtubule instability and axonal degeneration. Cell Rep. *6*, 93–103.

Nicastro, D., Schwartz, C., Pierson, J., Gaudette, R., Porter, M.E., and McIntosh, J.R. (2006). The molecular architecture of axonemes revealed by cryoelectron tomography. Science *313*, 944–948.

Nogales, E., Wolf, S.G., and Downing, K.H. (1998). Structure of the alpha beta tubulin dimer by electron crystallography. Nature *391*, 199–203.

Nogales, E., Whittaker, M., Milligan, R.A., and Downing, K.H. (1999). High-resolution model of the microtubule. Cell *96*, 79–88.

North, B.J., Marshall, B.L., Borra, M.T., Denu, J.M., and Verdin, E. (2003). The human Sir2 ortholog, SIRT2, is an NAD+-dependent tubulin deacetylase. Mol. Cell *11*, 437–444.

Odde, D. (1998). Diffusion inside microtubules. Eur. Biophys. J. *27*, 514–520.

Piperno, G., and Fuller, M.T. (1985). Monoclonal antibodies specific for an acetylated form of alpha-tubulin recognize the antigen in cilia and flagella from a variety of organisms. J. Cell Biol. *101*, 2085–2094.

Piperno, G., LeDizet, M., and Chang, X.J. (1987). Microtubules containing acetylated alpha-tubulin in mammalian cells in culture. J. Cell Biol. *104*, 289–302.

Poux, A.N., Cebrat, M., Kim, C.M., Cole, P.A., and Marmorstein, R. (2002). Structure of the GCN5 histone acetyltransferase bound to a bisubstrate inhibitor. Proc. Natl. Acad. Sci. USA *99*, 14065–14070.

Reed, N.A., Cai, D., Blasius, T.L., Jih, G.T., Meyhofer, E., Gaertig, J., and Verhey, K.J. (2006). Microtubule acetylation promotes kinesin-1 binding and transport. Curr. Biol. *16*, 2166–2172.

Roll-Mecak, A., and Vale, R.D. (2008). Structural basis of microtubule severing by the hereditary spastic paraplegia protein spastin. Nature *451*, 363–367.

Schulze, E., and Kirschner, M. (1987). Dynamic and stable populations of microtubules in cells. J. Cell Biol. *104*, 277–288.

Schulze, E., Asai, D.J., Bulinski, J.C., and Kirschner, M. (1987). Posttranslational modification and microtubule stability. J. Cell Biol. *105*, 2167–2177.

Shida, T., Cueva, J.G., Xu, Z., Goodman, M.B., and Nachury, M.V. (2010). The major alpha-tubulin K40 acetyltransferase alphaTAT1 promotes rapid ciliogenesis and efficient mechanosensation. Proc. Natl. Acad. Sci. USA *107*, 21517–21522.

Soppina, V., Herbstman, J.F., Skiniotis, G., and Verhey, K.J. (2012). Luminal localization of α-tubulin K40 acetylation by cryo-EM analysis of fab-labeled microtubules. PLoS ONE *7*, e48204.

Subramanian, R., Ti, S.C., Tan, L., Darst, S.A., and Kapoor, T.M. (2013). Marking and measuring single microtubules by PRC1 and kinesin-4. Cell *154*, 377–390.

Sui, H., and Downing, K.H. (2006). Molecular architecture of axonemal microtubule doublets revealed by cryo-electron tomography. Nature *442*, 475–478.

Tahirovic, S., and Bradke, F. (2009). Neuronal polarity. Cold Spring Harb. Perspect. Biol. *1*, a001644.

Takemura, R., Okabe, S., Umeyama, T., Kanai, Y., Cowan, N.J., and Hirokawa, N. (1992). Increased microtubule stability and alpha tubulin acetylation in cells transfected with microtubule-associated proteins MAP1B, MAP2 or tau. J. Cell Sci. *103*, 953–964.

Taschner, M., Vetter, M., and Lorentzen, E. (2012). Atomic resolution structure of human α-tubulin acetyltransferase bound to acetyl-CoA. Proc. Natl. Acad. Sci. USA *109*, 19649–19654.

Topalidou, I., Keller, C., Kalebic, N., Nguyen, K.C., Somhegyi, H., Politi, K.A., Heppenstall, P., Hall, D.H., and Chalfie, M. (2012). Genetically separable functions of the MEC-17 tubulin acetyltransferase affect microtubule organization. Curr. Biol. *22*, 1057–1065.

Varga, V., Leduc, C., Bormuth, V., Diez, S., and Howard, J. (2009). Kinesin-8 motors act cooperatively to mediate length-dependent microtubule depolymerization. Cell *138*, 1174–1183.

von Hippel, P.H., and Berg, O.G. (1989). Facilitated target location in biological systems. J. Biol. Chem. *264*, 675–678.

Webster, D.R., and Borisy, G.G. (1989). Microtubules are acetylated in domains that turn over slowly. J. Cell Sci. *92*, 57–65.

Wloga, D., and Gaertig, J. (2010). Post-translational modifications of microtubules. J. Cell Sci. *123*, 3447–3455.

Xiao, H., Verdier-Pinard, P., Fernandez-Fuentes, N., Burd, B., Angeletti, R., Fiser, A., Horwitz, S.B., and Orr, G.A. (2006). Insights into the mechanism of microtubule stabilization by Taxol. Proc. Natl. Acad. Sci. USA *103*, 10166–10173.

Yajima, H., Ogura, T., Nitta, R., Okada, Y., Sato, C., and Hirokawa, N. (2012). Conformational changes in tubulin in GMPCPP and GDP-taxol microtubules observed by cryoelectron microscopy. J. Cell Biol. *198*, 315–322.

Zhang, Y., Ma, C., Delohery, T., Nasipak, B., Foat, B.C., Bounoutas, A., Bussemaker, H.J., Kim, S.K., and Chalfie, M. (2002). Identification of genes expressed in C. elegans touch receptor neurons. Nature *418*, 331–335.

Ziółkowska, N.E., and Roll-Mecak, A. (2013). In vitro microtubule severing assays. Methods Mol. Biol. *1046*, 323–334.

EXTENDED EXPERIMENTAL PROCEDURES

Protein Expression and Purification

Homo sapiens TAT, residues 1-196 was expressed in *Escherichia coli* Rosetta2 (DE3) pLysS strain as a GST fusion. Protein expression was induced with 0.5 mM IPTG for 16 hr at 16°C. Cells were lysed using a microfluidizer and cellular debris was removed by centrifugation at 100,000 x *g* for 50 min. The protein was bound to GST resin (GE Healthcare) and released by overnight cleavage with Tobacco etch virus protease. Following cleavage, TAT was further purified by anion and cation exchange (Q and S sepharose, GE Healthcare). It was then concentrated and loaded on a HiLoad 16/60 S75 size exclusion column (GE Healthcare) pre-equilibrated with 25 mM Tris-HCl pH 7.5, 200 mM NaCl, 5mM $MgCl_2$, 2 mM tris(2-carboxyethyl phosphine). The *H. sapiens* TAT construct eluted as a symmetrical peak as a monomer at its expected molecular weight. All proteins were stored into single use aliquots and flash frozen in liquid nitrogen after addition of 15% glycerol.The human TAT numbering scheme is used throughout this study. *Danio rerio* TAT, residues 1-196, was expressed and purified as described in (Kormendi et al., 2012). Site directed mutagenesis was performed using Quickchange (Stratagene). The TAT mutants as well as the C-terminal GFP fusion protein were purified following the same protocol as for the wild-type *Danio rerio* TAT, residues 1-196 construct. *Xenopus laevis* stathmin with an N-terminal His-tag was expressed in *E. coli* and purified by affinity chromatography using a Ni-NTA column (QIAGEN) followed by size exclusion chromatography.

Peptide Acetylation Assays

Synthetic α-tubulin peptides (P1: GQMPSDKTIGGGDDSFNTFFSETGAG, P2: GQMPSDKTIGGGDDS and P3: GQMPSDKTIG, Biosynthesis) were dissolved in 20 mM HEPES/K pH 7.0 to a concentration of 10 mM, and the pH of the solution was adjusted to neutral pH with 5 M KOH. The N-terminal group was acetylated for all the substrate peptides used. Reaction mixtures consisted of 40 mM PIPES/KOH pH 6.9, 50 mM KCl, 1 mM DTT, 2 mM ac-CoA, 0.5 mM peptide and 0.089 μM TAT. After incubation at room temperature, aliquots were mixed with an equal volume of 0.1% trifluoroacetic acid and subjected to high-resolution liquid chromatography (HPLC) using a reversed phase analytical column from Vydac (218MS C18 5 mm, 25 × 0.46 cm). The product peptide contains a single acetyl group and is more hydrophobic than the substrate. This difference aided the separation of both peptides using RC HPLC with an acetonitrile gradient (5%–35% in 30 min for peptide P1, 5%–25% in 30 min for P2 and P3) in 0.05% trifluoroacetic acid as an eluent. The gradual conversion during the enzymatic reaction of a P2 substrate peptide to the product is illustrated in Figure S1A. Remaining peptide substrate and acetylated product were quantified by integration of the absorbance (220 nm) signals and the percentages of product formation versus time were calculated. Mass to charge ratio (m/z) of the acetylated peptides was determined by electrospray mass spectrometry and shows 42 mass units were added to the substrate (Figure S1A).

Acetylation Assays in the Presence of the Bisubstrate Peptide Analog

Bisubstrate peptide analogs were purchased from Biosynthesis and synthesized by the Fmoc [N-(9-fluorenyl)metoxycarbonyl] solid-phase method (Poux et al., 2002). Bromo carboxylic acids (R-2-bromopropionic acid and bromoacetic acid, for analog 1 and 2 respectively) were attached to the Lys residue on the resin after removing the Dde protective moiety of the ε-amino group. The bromo-carboxyamide intermediate peptides were cleaved from the resin and purified by reverse phase HPLC. Reaction of the CoASH with bromo-carboxyamide conjugates was performed in solution. Final bisubstrate analogs were subjected to reverse phase HPLC purification to homogeneity > 95% and mass spectrometry analysis. Small aliquots of the bisubstrate inhibitors were stored at −80°C in 20mM Tris pH 7.5 before crystallization and activity assays. Stock solutions of 10mM bisubstrate analogs were prepared in 20mM HEPES pH 7.5 and the pH was adjusted to 7.0 using 5 M KOH. *H. sapiens* TAT, residues 1-196, was incubated for 40 min at 4°C with analog 1. Reactions consisting of 10 μM tubulin, 2 μM TAT, 20 μM AcCoA, 20 μM colchicine and increasing concentration of bisubstrate analog 1 (0 mM, 0.1 mM, 0.2 mM, 0.5 mM, 1.0 mM) were assembled in 40 mM PIPES pH 6.9, 50 mM KCl, 1 mM EGTA, 1 mM DTT and assayed at room temperature. Acetylated tubulin levels were determined by western blot using antibodies specific to acetylated tubulin (clone 6-11B-1; 1:10000, Sigma-Aldrich). Western blots were quantified using ImageJ (National Institutes of Health). Activity was normalized to that in the absence of the analog. IC_{50} dose response fitting was plotted in Prism.

Crystallization and X-Ray Structure Determination

For crystallization, *H. sapiens* TAT was concentrated to 6 g/l and incubated with 4-fold molar excess tubulin peptide (Ac-Ser-Asp-Lys-Thr-NH_2) conjugated to CoA through the Lys side chain and propionic acid or acetic acid (Figure S1C). After 40 min incubation the sample was concentrated to 15 g/l. Crystals were obtained by hanging drop vapor diffusion at 21°C after mixing equal volumes of the protein and reservoir solutions (0.2 M Ammonium Acetate, 0.1 M Tris pH 8.5, 25% PEG 3350 (w/v)). Crystals grew with the symmetry of space group $P2_1$ with one TAT copy per asymmetric unit (analog 1: *a* = 37.1 Å, *b* = 52.5 Å, *c* = 50.3 Å, β = 106.8°; diffraction limit = 1.35Å; analog 2: *a* = 37.0 Å, *b* = 52.3 Å, *c* = 50.3 Å, β = 106.9°; diffraction limit = 1.35Å). The crystals were flash-frozen in liquid nitrogen and used for X-ray data collection (Advanced Light Source (ALS), beamline 5.0.1.).

The structures were solved by molecular replacement using PHASER (McCoy et al., 2007) with the apo tubulin acetyltransferase structure as the search model (Taschner et al., 2012). Iterative model building and refinement were carried out in COOT (Emsley and Cowtan, 2004) and PHENIX (Adams et al., 2010) for the structure with bisubstrate analog 1 and REFMAC (Murshudov et al., 2011) for the structure with bisubsrate analog 2, respectively. One region of the TAT polypeptide chain (residues 27-36) was not visible in the

electron density maps and is presumed disordered. The working and free R factors for the current TAT:bisubstrate analog 1 complex model at 1.35Å resolution are 13.1% and 16.8%, respectively (Table S1). The working and free R factors for the current TAT:bisubstrate analog 2 complex model at 1.35Å resolution are 14.8% and 17.3% (Table S1). MolProbity revealed no unfavorable (ϕ,ψ) combinations, and main chain and side-chain structural parameters consistently better than average.

Peptide Acetylation Assays
The acetylation assays with α-tubulin peptides exploit the increased hydrophobicity of the acetylated (product) peptide relative to the substrate to separate them through reverse-phase HPLC (Figure S1A).

Acetylation Assays with Tubulin and Tubulin Polymers
Acetylation of bovine brain tubulin (Cytoskeleton) was assayed by monitoring the incorporation of the radiolabeled acetyl group from [3H]-acetylCoA into tubulin as previously described (Kormendi et al., 2012). Reactions were performed at 10 μM final tubulin concentration and 1:5 molar ratio of TAT to tubulin. Reactions were assembled in buffer consisting of 80 mM PIPES pH 6.9, 50 mM NaCl, 1 mM EGTA, 1 mM MgCl$_2$, 1 mM DTT and 20 μM [3H]-acetyl-CoA (2.1 Ci/mmol), containing either 20 μM colchicine for the tubulin reactions or 1.6 M glycerol and 1 mM GTP for the microtubule reaction (microtubule dynamics are largely suppressed at the glycerol concentrations used (Manna et al., 2008)). Reactions were performed at room temperature (30°C for microtubules). The tubulin:stathmin assays were performed by adding 50 or 100 μM stathmin (1:5 or 1:10 tubulin:stathmin molar ratio, respectively). The assays were also performed with stathmin:tubulin complexes isolated by size exclusion chromatography and the results were the same. Tubulin dolastatin-10 rings were obtained by incubating 20 μM tubulin (Cytoskeleton) with 40 μM dolastatin-10 (NCI) for 45 min at room temperature in 80 mM PIPES pH 6.9, 50 mM KCl, 1 mM EGTA, 1 mM MgCl$_2$, 1 mM DTT. Taxol stabilized microtubules were prepared the day before and stored at room temperature. Tubulin Zn sheets were prepared as previously described (Nogales et al., 1998). Acetylated tubulin levels were determined by western blot using antibodies specific to acetylated tubulin (clone 6-11B-1; 1:10000, Sigma- Aldrich). Western blots were quantified using ImageJ (National Institutes of Health). TAT activity with Zn sheets was normalized to the value obtained for tubulin:colchicine in the same buffer as well as tubulin:stathmin in the same buffer. The presence of Zn sheets and dolastatin-10 rings in these reactions was confirmed by negative stain electron microscopy (Figure S3A). Unmodified tubulin was purified from tSA201 cells using a TOG1 affinity purification column as described in (Widlund et al., 2012). The lack of any tubulin posttranslational modifications on this purified tubulin was verified by mass spectrometry. *S. cerevisiae* tubulin was also purified using a TOG1 affinity purification column. Acetylation assays with subtilisin microtubules were performed at 1:100 TAT:tubulin molar ratio and acetylation was detected by western blot using antibodies specific to acetylated tubulin (clone 6-11B-1; 1:10000, Sigma- Aldrich) and IRDye 680LT anti-mouse IgG (1:18,000, Li-Cor) as a secondary antibody. Tubulin was detected using polyclonal rabbit anti-α tubulin antibody ab18251 (1:4000; Abcam) and an IRDye 800W anti-rabbit IgG (1:18,000, Li-Cor). Western blots were quantified using Image Studio Lite (Li-Cor).

Acetylation assays in the presence of various MAPs were performed at a 1:100 molar ratio of TAT:tubulin with Taxol stabilized microtubules (10 μM) preincubated at RT for 30 min with 20 μM human doublecortin (Bechstedt and Brouhard, 2012), 7 μM *Drosophila* spastin in the presence of 1 mM ATPγS to inhibit severing, but not microtubule binding (Roll-Mecak and Vale, 2008) and 17 μM motor domain of *Aspergillus nidulans* kinesin-5 in the presence of AMPPNP, respectively. The reactions were started by addition of ac-CoA. The extent of tubulin acetylation was determined using mouse monoclonal anti-acetylated tubulin antibody 6-11B-1 and IRDye 680LT anti-mouse IgG as a secondary antibody. Tubulin was detected using polyclonal rabbit anti-α tubulin antibody ab18251 and an IRDye 800W anti-rabbit. Western blots were quantified using Image Studio Lite (Li-Cor). Assays with subtilisin microtubules and DCX coated microtubules were also performed using radiolabeled acetyl group [3H]-acetylCoA. The results were identical to the ones performed using western blots.

Acetylation Assays with Bead-Conjugated TAT
A biotinylation tag (Beckett et al., 1999) (GGGLNDIFEAQKIEWHE) was introduced at the C terminus of the TAT construct. This construct was purified to homogeneity as described above. The purified TAT construct was biotinylated using biotin ligase (Genecopia). Electrospray mass spectrometry confirmed 100% completion of the biotinylation reaction with no traces of unbiotinylated TAT. 20 pmoles of biotinylated TAT was bound to 1 μm 200 μl Dynabeads MyOne Streptavidin C1 (Invitrogen) in reaction buffer consisting of 80 mM PIPES pH 6.9, 50 mM KCl, 1 mM EGTA, 1 mM MgCl$_2$, 1 mM DTT. Beads were washed five times with reaction buffer to remove any unconjugated TAT. Activity assays with colchicine tubulin and Taxol stabilized microtubules (10 μM) were performed and the extent of tubulin acetylation was determined using mouse monoclonal anti-acetylated tubulin antibody 6-11B-1 (1:10,000, Sigma-Aldrich) and anti-mouse peroxidase-conjugated antibody (1:1000, Cell Signaling) as a secondary antibody. Western blots were quantified using ImageJ (National Institutes of Health).

Microtubule Spin-Down Fluorescence Microscopy Assays and Image Analysis
Tubulin was deacetylated using *S. cerevisiae* Sirtuin 2 (Hst2) to lower background acetylation levels of brain tubulin. The deacetylation reaction contained 50 μM tubulin (Cytoskeleton), 5 μM yHst2 and 2 mM NAD$^+$ in assay buffer (80 mM PIPES 6.9, 1 mM MgCl$_2$, 1 mM EGTA) supplemented with 5 mM DTT and was allowed to proceed for two hours at room temperature after which tubulin was cycled once. The Sir2 inhibitor AGK2 (Outeiro et al., 2007) (Tocris Biosciences) was added to prevent further deacetylation.

Acetylation assays were performed with Taxol or glycerol stabilized microtubules. Taxol microtubules were prepared the day before and stored at room temperature. The acetylation reactions with Taxol-stabilized microtubules were performed in assay buffer supplemented with 50 mM KCl, 250 μM ac-CoA (or CoA for controls), 20μM AGK2, 10 μM Taxol, 4 μM tubulin and TAT at the desired TAT:tubulin molar ratios. Taxol microtubule acetylation assays were performed at room temperature. For the GTP/glycerol microtubule reactions, 50 μM tubulin in assay buffer, supplemented with 5 mM DTT, 1 mM GTP and 20% glycerol was incubated on ice for 5 min and then at 37°C for 1 hr to promote polymerization. Microtubules were then diluted into a prewarmed reaction mix. The final reaction mixture consisted of 4 μM tubulin in assay buffer supplemented with 20% glycerol, 5 mM DTT, 1 mM GTP, 20 μM AGK2, 250 μM ac-CoA (CoA in controls). A constant temperature of 37°C was maintained by using a blower (Nevtek). Reactions were started by TAT addition and samples were collected at the desired time points. Reactions were stopped by fixation with 1% glutaraldehyde, spun down onto poly-Lys coated coverslips as previously described (Murray, 1991) and stained with anti-acetylated tubulin antibodies (clone 6-11B-1, 1:400 dilution) and rabbit anti-tubulin antibodies (Synaptic Systems, 1:400 dilution) and visualized by staining with DyLight 488 goat anti-mouse and DyLight 549 goat anti-rabbit (Jackson Immunoresearch), respectively. A modified version of the TipTracker code (Demchouk et al., 2011) was used to find the microtubule backbones via Gaussian fit in the tubulin channel. Data corresponding to the backbones was inputted into a MATLAB code which used the pixel closest to the Gaussian peak and the nearest five neighbors on either side in the plane of the Gaussian fit to find the brightest pixel in the acetylated tubulin channel.

Specimen Preparation and Imaging by Transmission Electron Microscopy of Dolastatin-10 Rings and Antibody-Decorated Microtubules

Dolastatin-10 tubulin rings were obtained as previously described (Mulder et al., 2009). Dolastatin-10 (Concortis) was added to tubulin to 40 μM and the mixture was incubated at room temperature for 30 min. Dolastatin-10 rings were then incubated with TAT at the indicated concentrations. Specimens were prepared for electron microscopy using Cu 400-mesh grids covered with continuous carbon film and applying 3.3 μl of 0.5 μM rings and stained using 1% (w/v) uranyl formate followed by air-drying. Specimens were imaged on a FEI Morgagni 268 electron microscope operated at 80 kV and equipped with an AMT lens-coupled 1k x 1k CCD camera. For the comparison between TAT and TAT F105A, 0.4 μM dolastatin rings were incubated with TAT and TAT F105A at 1:10 molar ratio.

Taxol-stabilized microtubules were prepared by polymerizing glycerol-free porcine tubulin (Cytoskeleton) in the presence of 10% DMSO, 1 mM GTP and 5 μM Taxol in BRB80 buffer (80 mM PIPES pH 6.8, 1 mM MgCl$_2$, 1 mM EGTA) at 37°C for 30 min, after which Taxol was supplemented to a final concentration of 12.5 μM, and the polymerization reaction was transferred to room temperature. To achieve maximal acetylation, the preformed microtubules (5 μM) were treated with TAT (0.2 μM) in buffer AB (40 mM PIPES pH 5.8, 50 mM KCl, 0.5 mM MgCl$_2$, 0.8 mM EGTA, 2 mM DTT, 10 μM Taxol) and 0.25 mM ac-CoA. The reaction was allowed to proceed for 3.5 hr at 37°C. Next, unpolymerized tubulin and unbound TAT were removed by centrifugation in a TLA100.2 rotor at 35000 x g over a 60% glycerol cushion in BRB80 supplemented with 20 μM Taxol, and the pellet was resuspended in BRB80 supplemented with 20 μM Taxol. Microtubules were then mixed with 6-11B-1 antibody (Sigma) at a tubulin heterodimer:antibody stoichiometric ratio of 3:1 and incubated at room temperature for 15 min. Electron microscopy Cu 400 mesh grids (SPI Supplies) covered with continuous carbon film were prepared by spotting of 3 μl of microtubules followed by staining with 0.75% (w/v) uranyl formate and air-drying. Images were collected on a FEI Morgagni 268 microscope operated at 80 kV and equipped with an AMT lens-coupled 1k x 1k CCD camera. To look at the distribution of antibodies on microtubules of different lengths, grids were imaged on an Tecnai F20 electron microscope operated at 200 kV, and images were recorded automatically using the montage capabilities of SerialEM (Mastronarde, 2005) at 19000x nominal magnification, 2x binning, an electron dose of 4 electrons/Å^2 and 5 μm underfocus using an Ultrascan 4000 CCD. These imaging conditions correspond to a pixel size of 9.46Å on the specimen. The stitching together of micrographs was improved using the *blendmont* function in the software package IMOD (Kremer et al., 1996), which was also used for tracing and measuring microtubule lengths.

TIRF Imaging and Image Analysis

For single molecule assays microtubules were assembled from 1% tetramethyl-rhodamine labeled tubulin (Cytoskeleton TL590 M), 1% biotin labeled tubulin (Cytoskeleton T333P) and 98% porcine brain tubulin (Cytoskeleton T238P) and stabilized with 20 μM Taxol. Microtubules were immobilized on a glass surface using neutravidin (LifeTechnologies A-2666). TAT-GFP (50 nM) was perfused in assay buffer (80 mM PIPES 6.9, 1 mM MgCl$_2$, 1 mM EGTA, 50 mM KCl, 100 μM ac-CoA) supplemented with 1% F127 pluronic acid, 20 μM Taxol and oxygen scavengers to remove free oxygen from solution (Ziółkowska and Roll-Mecak, 2013).

Images were acquired using an inverted TIRF microscope (Nikon Ti-E with TIRF attachment). The excitation light was provided by a 488 nm Coherent cube for GFP and 532 nm Coherent Sapphire for TMR both operating at 20 mW before being coupled into an optical fiber and delivered to the microscope. A 100X 1.49 NA objective (Nikon CFI Apo TIRF 100X) was used to deliver the evanescent wave excitation light to the sample. The emitted light was collected by the same objective and split using an Andor TuCAM equipped with a dichroic mirror (Semrock Di02-R594) for splitting the emitted signal. The emitted fluorescence was imaged on two separate EMCCD cameras (Andor iXON3-897) equipped with the appropriate filters (Semrock FF01-514/30 for GFP and FF01-593/LP for TMR). The TuCAM introduces an additional 2x magnification factor yielding a final pixel size of 89 nm. Imaging was performed by first acquiring a single frame image of the TMR labeled microtubules using the 532 excitation channel for 200 ms; then, the 488 channel was used to image GFP-TAT at an exposure of 100 ms per frame for 1000 frames. The two channels were registered using a registration mask

created by imaging 100 nm tetraspeck beads and the ImageJ (National Institutes of Health) plugin bUnwarpJ. Images of GFP-TAT molecules were tracked using MTrackJ (Meijering et al., 2012) with the 7x7 bright centroid method. Tracks were generated by manually selecting the particle positions in subsequent frames until it disappeared. Tracks were excluded from analysis if: (i) the track remained stationary (these were rare events); (ii) the track started before the beginning of data collection; (iii) the microtubule end was reached before the particle detached; (iv) the tracks of adjacent molecules overlapped; (v) the track was shorter than 4 frames. The results of the tracking were imported into MATLAB and analyzed with a custom written script that extracts dwell times and scanned distances. The position data from multiple tracked particles (N = 192) were used to extract $< x^2 >$ versus time plot. Regression analysis was carried out in MATLAB. The linear regression used a weighted least-squares algorithm without a point at t = 0 and was not force-fit through zero. Images of TAT-GFP bound to a coverslip with no microtubules were used to calculate the bleaching time of GFP molecules and this was then used to correct the dwell time for the effects of bleaching (Figure S5A). Intensity analysis was performed using a 7x7 region of interest (ROI) to select molecules and measure their integrated intensity. A 7X7 ROI in a region adjacent to each particle was used to calculate the intensity of the background in the region of each selected particles and this background was subsequently subtracted to yield background subtracted particle intensities.

For the experiments on MAP coated microtubules, human doublecortin, *Drosophila* spastin and the motor domain of kinesin-5 BimC from *A. nidulans* were perfused at 1.2, 1 and 1 μM respectively into the chamber and allowed to incubate for 3 min before starting image acquisition. Concentrations as high as 2.5 μM were used for spastin without an effect on TAT-GFP scanning. For the dual color experiments, Taxol stabilized microtubules were decorated by addition of 85 nM, 135 nM and 270 nM DyLight 550 spastin, or a mixture of 500 nM unlabeled spastin with 20 nM DyLight 550 spastin in the presence of ATPγS (which inhibits severing, but not microtubule binding by spastin (Roll-Mecak and Vale, 2008)) and TAT-GFP was imaged as above at an exposure of 100ms per frame for 1000 frames.

Modeling TAT Diffusion

The TAT free diffusion coefficient is calculated from the Stokes-Einstein relationship, $D_0 = k_b T / 6\pi\eta R_H$, where k_b is the Boltzmann constant, T is the absolute temperature (T = 293 K), η is the viscosity of water at 293 K (10.02×10^{-4} kgm^{-1}s^{-1}) and R_H is the Stokes radius (2.2 and 2.7 nm for TAT and TAT-GFP, respectively, experimentally determined from analytical ultracentrifugation experiments and size exclusion chromatography, Figure S3B). The free diffusion coefficient of TAT is 79.3 μm^2/s. This indicates that a single TAT molecule travels an r.m.s. distance of 3.9 μm in ~0.1 s. TAT diffusion inside a microtubule is further hindered by the microtubule wall, resulting in a $D_{hindered}$ of 26.3 μm^2/s (2.3 μm traveled in 0.1 s), given by the Bungay-Brenner relationship (Bungay and Brenner, 1973):

$$D_{hinderd}/D_0 = 6\pi \left(\frac{9}{4}\pi^2\sqrt{2}(1-\lambda)^{-5/2} \left[1 - \frac{73}{60}(1-\lambda) + \frac{77,293}{50,400}(1-\lambda)^2 \right] - 22.5083 - 5.6117\lambda - 0.3363\lambda^2 - 1.216\lambda^3 + 1.647\lambda^4 \right)^{-1}$$

where λ is the ratio of the molecular radius of TAT to the microtubule inner radius ($\lambda = 0.36$). Thus, the hindrance effect due to the microtubule wall results in ~3-fold reduction in TAT diffusivity. However, TAT diffusion is most significantly retarded by its reversible binding to the microtubule lumen (Odde, 1998). This results in a final effective diffusion constant of TAT given by:

$$D_{effective} = \frac{D_{hindered}}{1 + \frac{n}{K_d}}$$

where K_d is the dissociation equilibrium constant and n is the maximum bound TAT concentration (luminal TAT capacity). This relationship applies only in cases where [TAT] < K_d (Crank, 1975; Odde, 1998)). Using n = 14.1 mM, and K_d = 44 μM as measured from microtubule sedimentation assays, $D_{effective}$ ~0.082 μm^2/s. TAT concentration profiles were calculated using Fick's second law (Crank, 1975; Odde, 1998) and the diffusion coefficient for TAT.

SUPPLEMENTAL REFERENCES

Adams, P.D., Afonine, P.V., Bunkóczi, G., Chen, V.B., Davis, I.W., Echols, N., Headd, J.J., Hung, L.W., Kapral, G.J., Grosse-Kunstleve, R.W., et al. (2010). PHE-NIX: a comprehensive Python-based system for macromolecular structure solution. Acta Crystallogr. D Biol. Crystallogr. *66*, 213–221.

Beckett, D., Kovaleva, E., and Schatz, P.J. (1999). A minimal peptide substrate in biotin holoenzyme synthetase-catalyzed biotinylation. Protein Sci. *8*, 921–929.

Crank, J. (1975). The Mathematics of Diffusion, Second Edition (London, UK: Oxford University Press).

Demchouk, A.O., Gardner, M.K., and Odde, D.J. (2011). Microtubule tip tracking and tip structures at the nanometer scale using digital fluorescence microscopy. Cell Mol. Bioeng. *4*, 192–204.

Emsley, P., and Cowtan, K. (2004). Coot: model-building tools for molecular graphics. Acta Crystallogr. D Biol. Crystallogr. *60*, 2126–2132.

Kremer, J.R., Mastronarde, D.N., and McIntosh, J.R. (1996). Computer visualization of three-dimensional image data using IMOD. J. Struct. Biol. *116*, 71–76.

Manna, T., Honnappa, S., Steinmetz, M.O., and Wilson, L. (2008). Suppression of microtubule dynamic instability by the +TIP protein EB1 and its modulation by the CAP-Gly domain of p150glued. Biochemistry *47*, 779–786.

Mastronarde, D.N. (2005). Automated electron microscope tomography using robust prediction of specimen movements. J. Struct. Biol. *152*, 36–51.

McCoy, A.J., Grosse-Kunstleve, R.W., Adams, P.D., Winn, M.D., Storoni, L.C., and Read, R.J. (2007). Phaser crystallographic software. J. Appl. Cryst. *40*, 658–674.

Murray, A.W. (1991). Cell cycle extracts. Methods Cell Biol. *36*, 581–605.

Murshudov, G.N., Skubák, P., Lebedev, A.A., Pannu, N.S., Steiner, R.A., Nicholls, R.A., Winn, M.D., Long, F., and Vagin, A.A. (2011). REFMAC5 for the refinement of macromolecular crystal structures. Acta Crystallogr. D Biol. Crystallogr. *67*, 355–367.

Outeiro, T.F., Kontopoulos, E., Altmann, S.M., Kufareva, I., Strathearn, K.E., Amore, A.M., Volk, C.B., Maxwell, M.M., Rochet, J.C., McLean, P.J., et al. (2007). Sirtuin 2 inhibitors rescue alpha-synuclein-mediated toxicity in models of Parkinson's disease. Science *317*, 516–519.

Widlund, P.O., Podolski, M., Reber, S., Alper, J., Storch, M., Hyman, A.A., Howard, J., and Drechsel, D.N. (2012). One-step purification of assembly-competent tubulin from diverse eukaryotic sources. Mol. Biol. Cell *23*, 4393–4401.
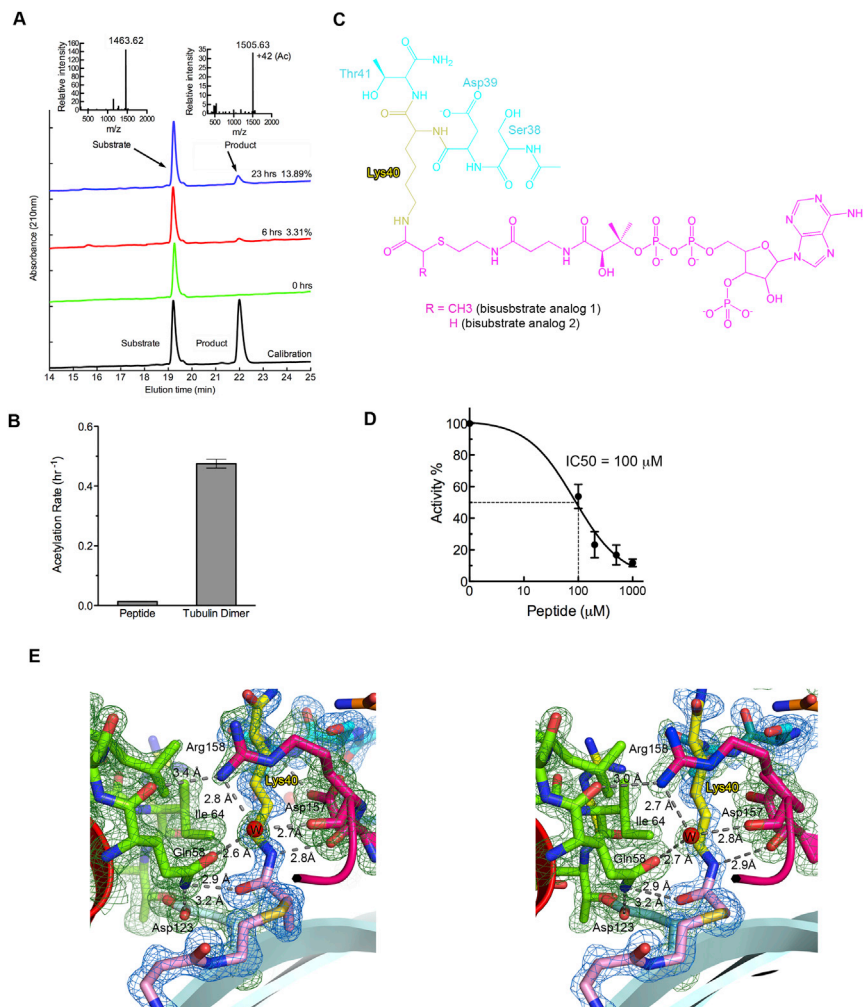
Figure S1. TAT Acetylation Activity with Tubulin Peptide and Bisubstrate Analog, Related to Figure 1

(A) HPLC assay for α−tubulin peptide acetylation. HPLC traces showing the progression of the acetylation reaction monitored by the appearance and gradual increase in the absorbance of the elution peak for the acetylated peptide and the simultaneous decrease in the total absorbance of the elution peak of the substrate peptide from a C18 reversed phase high-performance liquid chromatography column. Insets show mass spectra of the substrate and product peptide.

(B) TAT acetylation activity with a ten-residue Lys40 peptide and tubulin. TAT activity is not higher with longer peptides of up to 26 residues (data not shown).

(C) Chemical structure of the two bisubstrate analogs used in this study. The CoA moiety is shown in pink, Lys40 in yellow and the rest of the tubulin peptide moiety in cyan. The existence of a ternary complex between TAT, acetyl-CoA and its tubulin substrate is supported by previous kinetic analyses (Friedmann et al., 2012).

(D) IC_{50} curve for bisubstrate analog 1 used in this study. (E) Close-up of the active site of the TAT complex structure showing the bisubstrate analog 1 (left panel) or bisubstrate analog 2 (right panel) as a stick representation and the |Fo|-|Fc| density contoured at 3.5σ (blue) before modeling the ligand and the 2|Fo|-|Fc| omit map density contoured at 1.5σ (green). Secondary structure elements colored as in Figure 1A; hydrogen bonds shown as dashed gray lines.
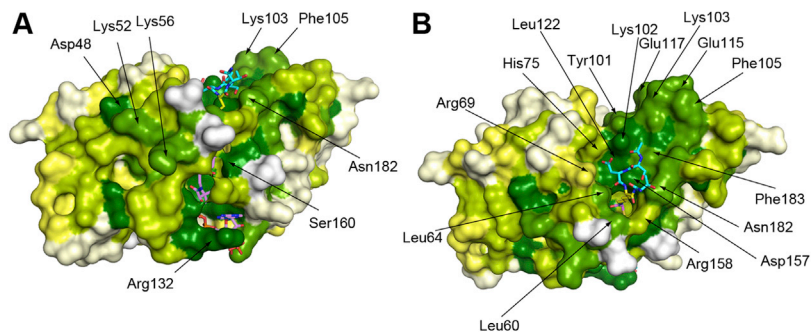
Figure S2. TAT Interaction Surface with Tubulin, Related to Figure 2

(A) Active site view of the TAT molecular surface color-coded for conservation on a gradient from white (40% identity) to green (100% identity). Bisubstrate analog in stick representation colored as in Figures 1 and S1C.

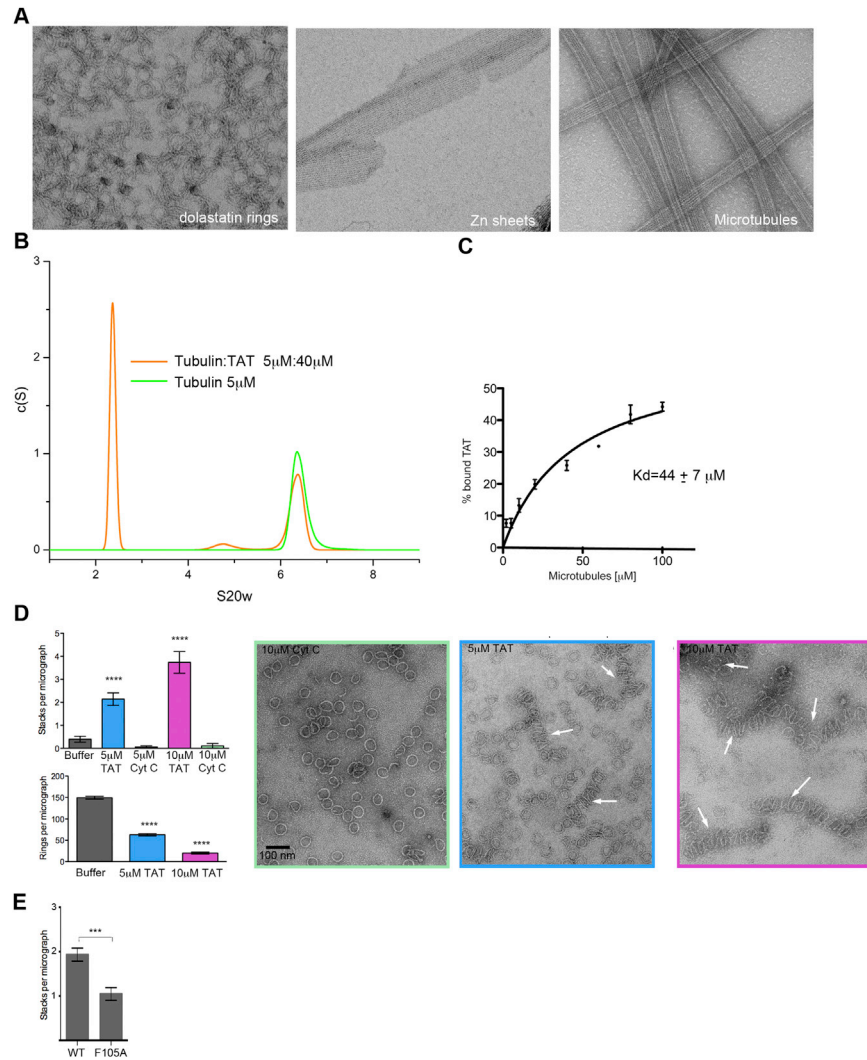(B) Peptide and tubulin binding site view (90° rotated from A). Colored as in A.

Figure S3. TAT Binding to Tubulin and Microtubules, Related to Figure 3

(A) Representative negative stain electron micrographs of tubulin substrates (left to right: dolastatin rings, Zn sheets and microtubules) used in acetylation assays shown in Figure 3.

(B) Analytical ultracentrifugation of tubulin and tubulin:TAT mixtures at the indicated concentrations. The low s value peak represents TAT alone. No peak with s value higher than tubulin is observed indicating the absence of a stable tubulin:TAT complex at these concentrations.

(C) TAT binding to Taxol-stabilized microtubules.

(D) TAT promotes the formation of stacks of dolastatin rings. Quantification of tubulin rings and stacks from randomly selected negative stain EM micrographs (n = 15 micrographs) obtained in the presence of TAT and Cytochrome C (Cyt C) as a negative control. Shown are average values ± SEM. Panels from left to right: fields of dolastatin-10 tubulin rings after incubation with Cytochrome C or TAT at the indicated concentrations. Arrows point to stacks. ****$p < 0.0001$, t test.

(E) Quantification of stacks from randomly selected negative stain EM micrographs (n = 13 micrographs) obtained with TAT and a mutant impaired in microtubule acetylation. Shown are average values ± SEM. ***$p < 0.001$, t test.
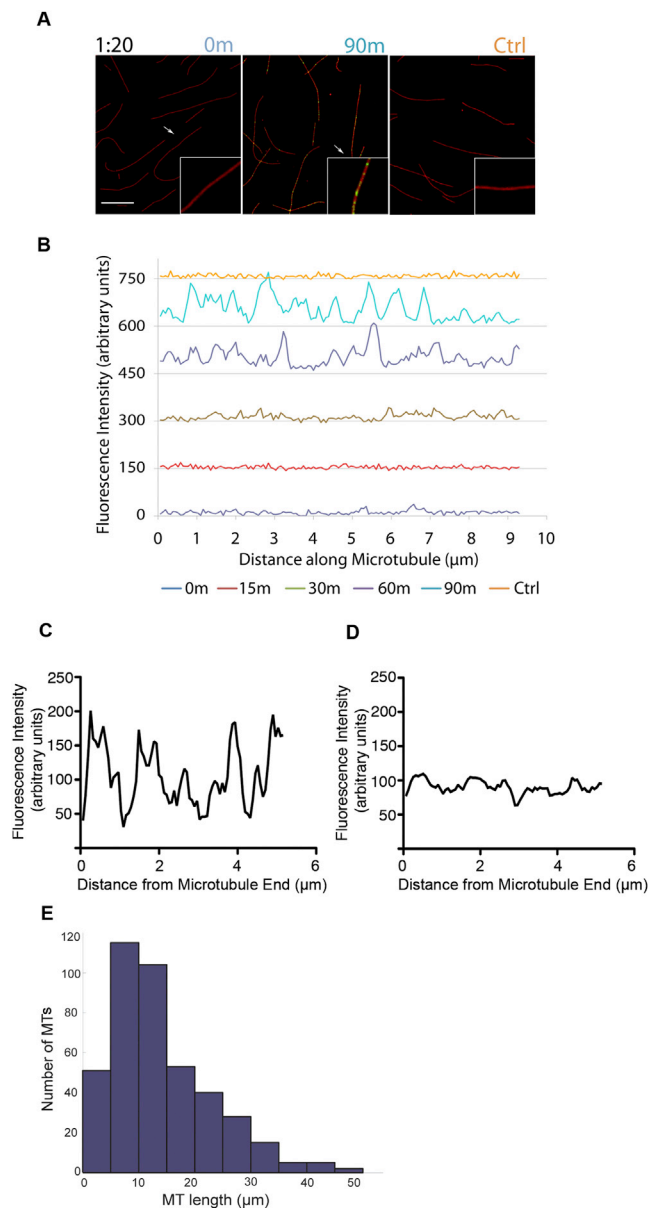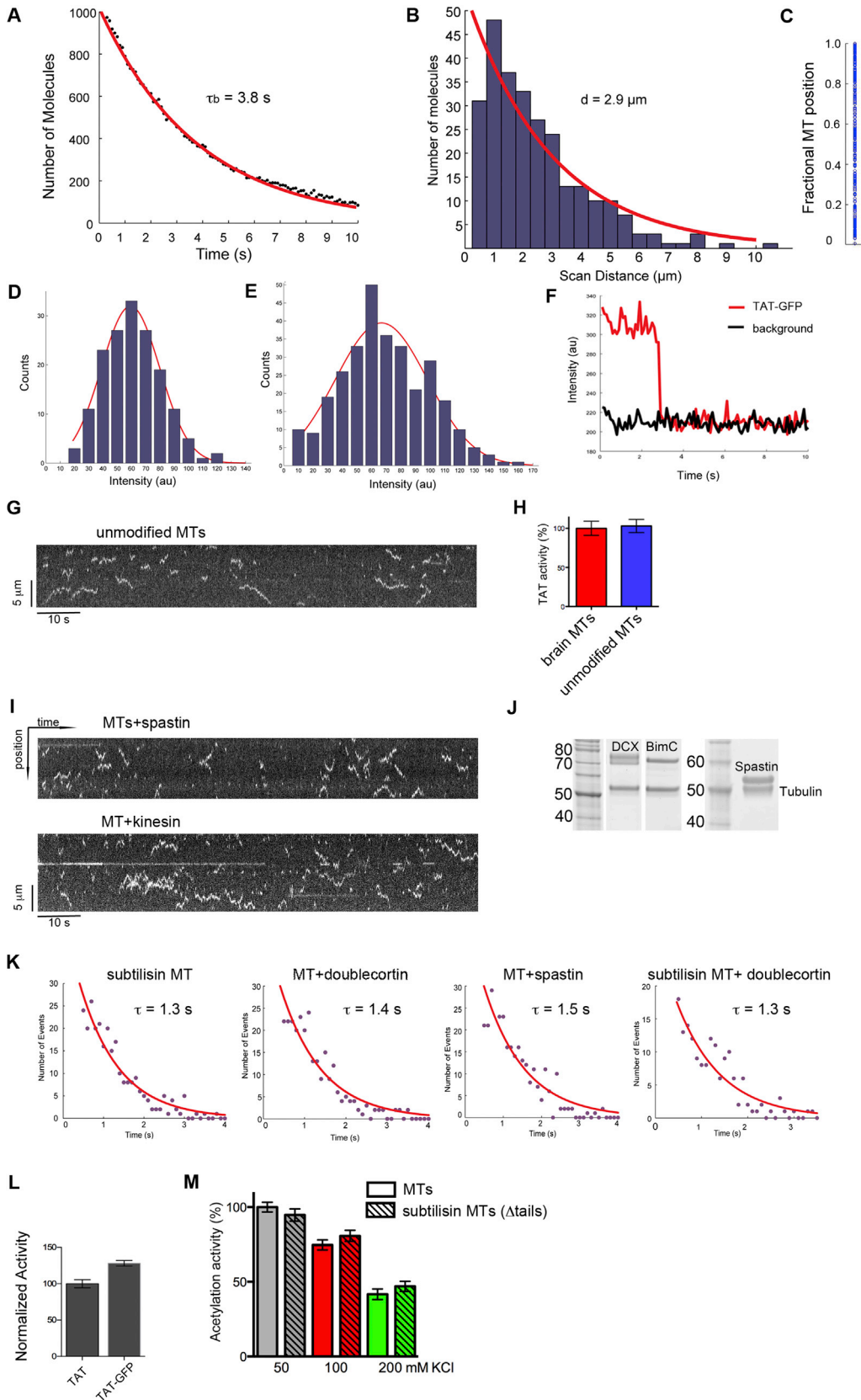
Figure S4. Microtubule Acetylation Occurs Stochastically along the Entire Microtubule Length and Is Not Biased for Microtubule Ends, Related to Figure 4

(A) Time course of non-Taxol stabilized glycerol microtubules stained for tubulin (red) and acetylated tubulin (green) after addition of TAT at a 1:20 TAT:tubulin molar ratio. Close-ups of selected microtubules (arrows) are shown in insets; scale bar 5 μm.

(B) Line-scans of selected microtubules (arrows) from panel A in the acetylated tubulin channel. Line-scans from successive time points are staggered vertically by 150 units for clarity.

(C and D). Analysis of acetylation near microtubule ends at a 1:20 TAT:tubulin molar ratio. (C) Representative scan of the terminal 5μm of a microtubule. (D) Average of 28 line-scans of microtubule ends from the tip to 5μm into the microtubule. Microtubules scanned had a minimum length of 10 μm.

(E) Representative histogram of microtubule length distributions for samples used in acetylation reactions shown in Figure 4.

(legend on next page)

Figure S5. Single-Molecule Fluorescence Characterization of the TAT-Microtubule Interaction, Related to Figure 5

(A) Distribution of surface bound TAT-GFP molecules over time. The number of surface-bound molecules (black dots) decays exponentially as the GFP is bleached. An exponential decay fit (red line) gives a time constant of 3.8 s (R^2 = 0.99).

(B) Histogram of scan distances for TAT-GFP molecules. The distribution was fitted to a single exponential decay function and yielded a mean scan length of 2.9 μm (R^2 = 0.89).

(C) Initial positions (blue dots) of scanning TAT-GFP molecules along one microtubule imaged at an exposure of 100ms per frame for 5000 frames.

(D) Initial fluorescence intensity distribution of TAT particles on microtubules showing a Gaussian distribution around a mean consistent with a single TAT-GFP molecule.

(E) Initial fluorescence intensity distribution of TAT-GFP particles immobilized on glass showing a monodisperse profile.

(F) One-step photobleaching trace of immobilized TAT-GFP consistent with each molecule existing as a monomer over the exposure time (100 ms).

(G) Kymograph depicting the motion of single TAT-GFP molecules on unmodified microtubules.

(H) Comparison of TAT acetylation activity on posttranslationally modified microtubules purified from brain tissue and unmodified microtubules purified from tSA201 cells (the absence of posttranslational modifications was verified by mass spectrometry).

(I) Kymographs depicting the motion of TAT-GFP on brain microtubules in the presence of saturating amounts of *Drosophila* spastin and 1 mM ATPγS (top) or the GST fusion of the motor domain of kinesin-5 BimC from *Apergillus nidulans* (Cytoskeleton) in the presence of 1mM AMPPNP (bottom).

(J) SDS-PAGE gels showing that under conditions similar to those used in our single-molecule experiments the various MAPs saturated the microtubules (doublecortin, spastin, and kinesin-5 motor domain). Doublecortin was added at 1 μM; spastin at 1 μM in the presence of 1 mM ATPγS, and the GST fusion of the kinesin-5 motor domain at 1 μM in the presence of 1 mM AMPPNP/

(K) Left to right: distributions of durations of TAT-GFP interactions with subtilisin treated microtubules that miss both the α- and β C-terminal tails (complete digestion was verified by mass spectrometry), microtubules decorated with saturating amounts of doublecortin, microtubules decorated with saturating amounts of spastin in the presence of 1 mM ATPγS and subtilisin microtubules decorated with doublecortin. τ is the mean interaction lifetime obtained by fitting an exponential curve to the histogram and correcting for photobleaching (R^2 = 0.94 for subtilisin MT; R^2 = 0.90 for MT+doublecortin; R^2 = 0.86 for MT+spastin and R^2 = 0.87 for subtilisin MT+doublecortin).

(L) Activity of TAT-GFP fusion construct with microtubules.

(M) TAT acetylation activity with microtubules (MTs) and microtubules missing their C-terminal tails after treatment with subtilisin (subtilisin MTs (Δtails)) at various ionic strengths, showing that the sensitivity to high ionic strength is not dependent on the presence of the tubulin C-terminal tails.
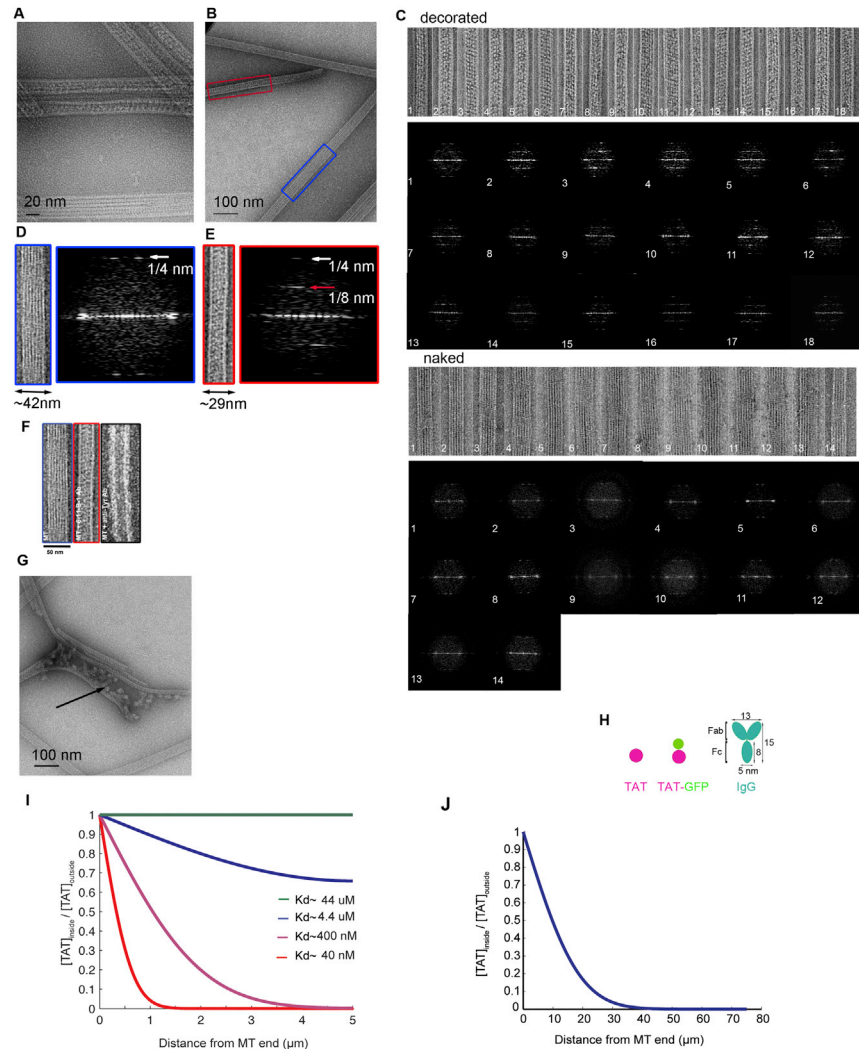
Figure S6. Entry to the Microtubule Lumen, Related to Figure 6

(A–H) Antibodies recognizing the acetylated tubulin loop enter the microtubule lumen. (A), (B) Fields of TAT-acetylated Taxol-stabilized microtubules incubated with antibody (6-11B-1) specific for acetylated tubulin. Boxes indicate individual naked (blue) and decorated (red) microtubules, boxed out for analysis in D and E. (C) Selected microtubules and their diffraction patterns indicating two populations of microtubules, antibody decorated (top) and naked (bottom). (D), (E) Apparent outer diameters of boxed microtubules from panel B and corresponding diffraction patterns are shown for naked (D) and decorated microtubules (E) respectively. The naked microtubules are flattened during grid preparation (outer diameter, OD ~42 nm) and give rise to the characteristic 4 nm layer-line (white arrow) because the underlying helical structure has a 4 nm spacing at the low resolution of negative-stain EM due to α/β tubulin equivalency. The decorated microtubule (outer diameter, OD ~29 nm) produces a distinct, additional 8 nm layer-line (red arrow) indicative of the regular binding of the acetylated Lys40-directed antibody to the tubulin heterodimer. These decorated microtubules showed no additional density along the edges, indicating that the binding occurs on the luminal surface. The luminal decoration is also in agreement with our observation that the decorated microtubules undergo minimal flattening, probably because their lumen is filled with antibody, which supports them during grid preparation. Analysis of 42 decorated microtubules (80 microtubule out of 122 total microtubules showed no visible decoration) revealed that the antibody decoration was either complete (71% of microtubules) or proceeding from the ends (29%). We observed no undamaged microtubules with internal antibody decoration that was also not observed along the length of the microtubule and no microtubules longer than 6 μm showed complete decoration throughout their entire lengths. These data suggest that the antibody is able to diffuse into the lumen from microtubule ends. (F) Comparison of naked microtubules (left panel), microtubules decorated with the antibody specific for Lys40 acetylation (middle panel) and microtubules decorated with an antibody specific for the tyrosinated α-tubulin tail located on the outside of the microtubule (right panel). While the microtubule decorated with the anti-acetylation antibody is narrower and shows no density on the microtubule surface, the anti-Tyr tubulin decorated microtubule shows a halo of antibodies decorating the microtubule surface. (G) Clusters of antibodies (black arrows) at sites of microtubule damage where the luminal surface is exposed. (H) Cartoon depiction of relative physical dimensions of TAT, TAT-GFP and IgG molecules shown at the same scale. The microtubule inner diameter is 15 nm.

(I) The effect of microtubule binding affinity on calculated diffusion profiles inside the lumen of a 10 μm-long microtubule after 10 min for a particle of TAT dimensions. Microtubule affinities of 40 nM, 400 νM, 4.4 μM and 44 μM were used.

(J) Calculated profile of TAT diffusion into a microtubule at 10 min. Diffusion was considered rate limiting at a microtubule length where TAT concentration inside the lumen was less than 1% the outside TAT concentration at the midpoint of the tube.